

Deep multi-frequency radio imaging in the Lockman Hole using the GMRT and VLA: I. The nature of the sub-mJy radio population

Edo Ibar,^{1,2*} R. J. Ivison,^{1,2} A. D. Biggs,^{1,3} D. V. Lal,⁴ P. N. Best² and D. A. Green⁵

¹ UK Astronomy Technology Centre, Royal Observatory, Blackford Hill, Edinburgh EH9 3HJ

² Institute for Astronomy, University of Edinburgh, Blackford Hill, Edinburgh EH9 3HJ

³ European Southern Observatory, Karl-Schwarzschild-Str. 2, D-85748 Garching, Germany

⁴ Institute of Astronomy and Astrophysics, Academia Sinica, P.O. Box 23-141, Taipei 10617, Taiwan

⁵ Astrophysics Group, Cavendish Laboratory, 19 J. J. Thomson Avenue, Cambridge CB3 0HE

DRAFT DATED: 20 MARCH 2009

ABSTRACT

In the run up to routine observations with the upcoming generation of radio facilities, the nature of sub-mJy radio population has been hotly debated. Here, we describe multi-frequency data designed to probe the emission mechanism that dominates in these faint radio sources. Our analysis is based on observations of the Lockman Hole using the Giant Metre-wave Radio Telescope (GMRT) – the deepest 610-MHz imaging yet reported – together with 1.4-GHz imaging from the Very Large Array (VLA), well matched in resolution and sensitivity to the GMRT data ($\sigma_{610\text{MHz}} \sim 15 \mu\text{Jy beam}^{-1}$, $\sigma_{1.4\text{GHz}} \sim 6 \mu\text{Jy beam}^{-1}$, FWHM $\sim 5 \text{ arcsec}$). The GMRT and VLA data are cross-matched to obtain the radio spectral indices for the faint radio emitters. Statistical analyses show no clear evolution for the median spectral index, $\alpha_{1.4\text{GHz}}^{610\text{MHz}}$ (where $S_\nu \propto \nu^\alpha$), as a function of flux density. $\alpha_{1.4\text{GHz}}^{610\text{MHz}}$ is found to be approximately -0.6 to -0.7 , based on an almost unbiased $10-\sigma$ criterion, down to a flux level of $S_{1.4\text{GHz}} \gtrsim 100 \mu\text{Jy}$. The fraction of inverted spectrum sources ($\alpha_{1.4\text{GHz}}^{610\text{MHz}} > 0$) is less than 10 per cent. The results suggest that the most prevalent emission mechanism in the sub-mJy regime is optically-thin synchrotron, ruling out a dominant flat spectrum or ultra-steep spectrum radio population. The spectral index distribution has a significant scatter, $\Delta\alpha \approx 0.4 - 0.5$, which suggests a mixture of different populations at all flux levels. Spectroscopic classification of radio sources with X-ray emission has allowed us to estimate that the fraction of radio-quiet AGN at $30 \mu\text{Jy} \lesssim S_{1.4\text{GHz}} < 300 \mu\text{Jy}$ is roughly 25 ± 10 per cent, suggesting that star-forming galaxies dominate the sub-mJy regime.

Key words:

1 INTRODUCTION

In early studies, radio astronomy was limited to bright sources associated with rare luminous ($L_{1.4\text{GHz}} \approx 10^{25-29} \text{ W Hz}^{-1}$) radio galaxies and quasars (QSOs). Galaxies with nuclear activity are usually characterised by powerful radio lobes, which are evidence of interactions between highly collimated relativistic flows – coming from the nuclear activity – and the interstellar/intergalactic medium. These magnificent radio-loud structures were classified by Fanaroff & Riley (1974) depending on their shape (FR I and II classes), and optical identifications showed that these active galactic nuclei (AGN) are usually hosted by massive elliptical galaxies (Matthews et al. 1964). It was not until the 1980s that radio source counts at the sub-mJy level revealed a new radio population (Windhorst et al. 1985; Mitchell & Condon 1985). The nature

of the faint radio sources which dominate the number counts below $\sim 1 \text{ mJy}$ is controversial. Various studies (e.g. Simpson et al. 2006; Seymour et al. 2008; Smolčić et al. 2008) have identified this population with star-forming galaxies (starbursts, spirals or irregulars) and radio-quiet AGN (faint FR I, Seyfert galaxies).

The fractions of AGN and star-forming galaxies that contribute to the sub-mJy radio regime is still hotly debated. Many different approaches have been taken to disentangle these two populations: using far-infrared (far-IR)/radio flux ratios (Donley et al. 2005; Ibar et al. 2008); tackling their radio brightness temperatures and luminosities (Wrobel et al. 2005; Garrett et al. 2005); resolving their radio morphologies (Muxlow et al. 2005; Biggs & Ivison 2008); identifying optical host galaxies via morphology (Padovani et al. 2007), or spectroscopy (Gruppioni et al. 1999; Barger et al. 2007), or their locus in colour-colour diagrams (Ciliegi et al. 2005); via X-ray identifications (Simpson et al. 2006); or using their radio spectral indices (Richards 2000;

* e-mail: ibar@roe.ac.uk

Clemens et al. 2008). These approaches tend to yield substantially different results.

In terms of spectral indices, α , star-forming galaxies are usually considered to have a mean spectral index between -0.8 and -0.7 (where $S \propto \nu^\alpha$), with a relatively small dispersion, 0.24 (Condon 1992). A sample of $z < 0.5$ FR I & II sources have also been found to have similar spectral indexes (between 178 MHz and 750 MHz), with mean and scatter of $\alpha = 0.74 \pm 0.19$ and $\alpha = 0.79 \pm 0.14$, respectively (Laing et al. 1983). This implies that studies based on the radio spectral index have large difficulties disentangling star-forming from steep-spectrum FR-AGN populations. Nevertheless, the radio spectral index is sensitive to core-dominated radio-quiet AGN (Blundell & Kuncic 2007), GHz-peaked sources (GPS; Gopal-Krishna et al. 1983; O'Dea 1998; Snellen et al. 2000) and the ultra-steep spectrum sources (USS; Rottgering et al. 1994; Chambers et al. 1996; Jarvis et al. 2001) usually found at high redshift.

Recent studies, combining 610 -MHz and 1.4 -GHz data, have found evidence for flatter spectral indices (Bondi et al. 2007; Garn et al. 2008a) and larger dispersions at sub-mJy radio fluxes (e.g. Magliocchetti et al. 2008), suggesting that core-dominated radio-quiet AGN are playing a key role in the sub-mJy radio population.

In this paper, we present two very deep radio images centred on the Lockman Hole (LH): the deepest to date at 610 MHz ($\sigma \sim 15 \mu\text{Jy beam}^{-1}$) obtained using the Giant Metrewave Radio Telescope (GMRT), and a deep 1.4 -GHz image ($\sigma \sim 6 \mu\text{Jy beam}^{-1}$) obtained using the Very Large Array (VLA). At these long wavelengths the dominant powering process is synchrotron radiation. We merge the two datasets to characterise the spectral index of the μJy radio population as a function of flux density, thereby probing the physical mechanisms that dominate in this enigmatic radio population: optically thin (steep spectrum) or self-absorbed (hard spectrum) synchrotron emission. Our deep, well-matched observations – about three times deeper than previous data – mitigate the well-known bias towards the detection of steeper spectra at longer wavelengths, or flatter spectra at shorter wavelengths. This work provides a parameterisation of the radio spectral energy distribution (SED) that can be used to estimate more precise k -corrections for the observed radio emitters.

Throughout this paper we assume a Universe with $\Omega_m = 0.27$, $\Omega_\Lambda = 0.73$ and $H_0 = 71 \text{ km s}^{-1} \text{ Mpc}^{-1}$.

2 RADIO OBSERVATIONS

2.1 GMRT

During six 12-hr sessions in 2006 February and July we obtained data for three pointings (primary beam FWHM ~ 43 arcmin) in the Lockman Hole (see Table 1), separated by 11 arcmin (LOCKMAN-E, LOCK-3, LHEX4), typically with 28 of the 30 antennas that comprise the GMRT,¹ near Pune, India. The total integration time in each field, after overheads, was 16 hr. We recorded 128 channels ($\Delta\nu = 16$ MHz each) centred on 610 MHz every 16 s integration in the lower and upper sidebands (LSB and USB centred at 602 and 618 MHz, respectively) in each of two polarisations. Integrations of 40 -min duration were interspersed with 5 -min scans of the nearby calibrator, $1035+564$ ($S_{610\text{MHz}} \approx 2$ Jy), with scans of

¹ GMRT is run by the National Centre for Radio Astrophysics of the Tata Institute of Fundamental Research.

$3C\,48$, $3C\,147$ and $3C\,286$ ($S_{610\text{MHz}} = 29.4$, 38.3 and 21.1 Jy, respectively) for flux and bandpass calibration.

Calibration initially followed standard recipes within *ATPS*, using FITLD, INDXR and SETJY. However, because of concerns that some baselines were picking up signal from local power lines and that $1035+564$ might be too weak to act as a reliable secondary flux calibration source, a raft of new measures were introduced to avoid detrimental effects on the resultant images.

For each session, the bright source least affected by radio-frequency interference (RFI) and with the fewest malfunctioning antennas was SPLIT and chosen to be the primary flux density and bandpass calibrator. After intensive manual flagging of RFI using SPFLG and TVFLG, the chosen calibrator was self-calibrated in phase. Antenna-based bandpass solutions were determined, copied to the full dataset and used to determine new gain solutions for the primary calibrator. The gain and bandpass solutions were then applied to the entire dataset with no time-dependent corrections. The secondary calibrator was employed to identify problems with the antennas rather than to track changes in gain, although a more conventional approach was used to generate images with good positional information for use in initial phase self-calibration.

Next, calibrated data were processed with the FLGIT RFI-rejection algorithm. Each 128 -channel integration was split into a series of seven 15 -channel pieces, discarding the first 10 and last 13 channels, and points deviating from linear fits to each piece by more than 5σ were rejected. Data brighter than $1.5 \times$ the brightest calibrator were also rejected, leaving around 70 to 95 per cent of the original data intact, depending on the severity of the RFI.

The resulting data, now somewhat cleaner, were averaged down to yield 15 channels in each polarisation for each session, pointing and sideband: a total of 12 dual-polarisation, single-sideband, single-source datasets.

Before imaging, a specially modified version of UVAVG (now standard) was employed to determine and subtract the average value for each baseline and channel throughout the entire session (hence the need for time-independent calibration in the preceding steps).

Imaging each of these datasets entailed the creation of a mosaic of 37 facets, each 512^2 pixels (1.25^2 arcsec^2 per pixel), to cover the primary beam. A further 6 – 12 bright sources outside these central regions, identified in heavily tapered maps, were also imaged. Our aim was to obtain the best possible model of the sky. CLEAN boxes were placed tightly around all radio sources for use in self-calibration, first in phase alone (SOLMODE = 'A!P'), then in amplitude and phase (SOLMODE = 'A&P'), with a solution interval of 2 min, staggered by 1 min. The uv data were weighted using RO-BUST = -0.5 , UVRANGE = 0.8 , $100 \text{ k}\lambda$ and UVTAPER = 28 , $28 \text{ k}\lambda$ with UVBOX = 5 .

After CLEAN components were subtracted from the uv data, more manual flagging was applied, as well as another pass through the UVAVG task and a clip at the 350 -mJy level using UVFLG (now CLIP). CLEAN components were re-introduced (UVSUB, FACTOR = -1), then data with common sidebands from February and July were combined using DBCON to reduce the variation in beam size and shape amongst the datasets.

The final six mosaics (see Table 1), two for each pointing (LSB and USB), were then convolved to a common beam size ($7.1 \text{ arcsec} \times 6.5 \text{ arcsec}$, with the major axis at position angle 70°). The noise (see Table 1) from each image is estimated and introduced in their headers using IMEAN, before all are knitted together using FLATN. An appropriate correction was made for the attenuation of the primary beam, with data rejected at radii beyond where

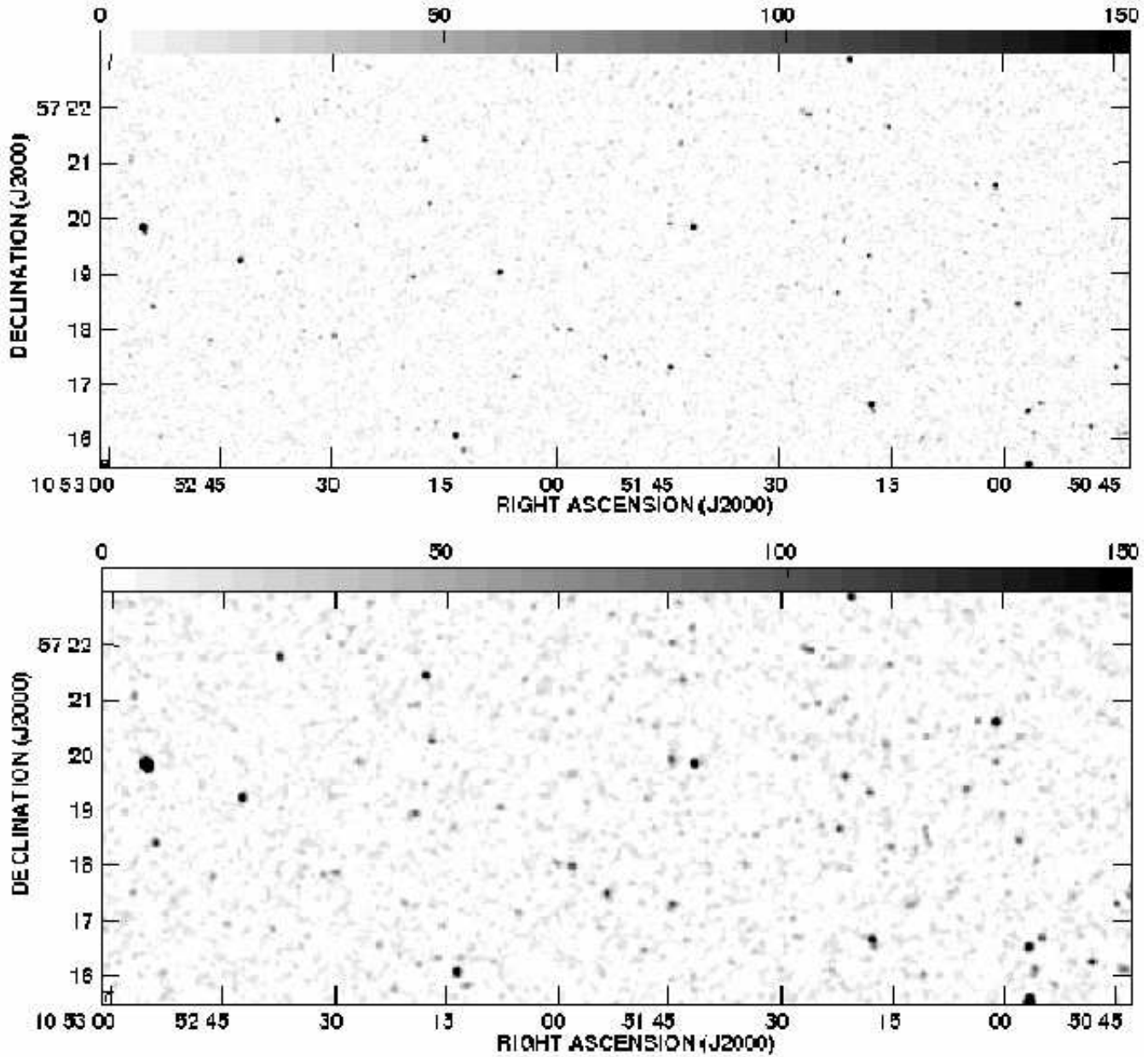


Figure 1. Top: A small region (18.7×7.5 arcmin 2) near the centre of the 1.4-GHz mosaic. The linear grey-scale runs from 0 to $150 \mu\text{Jy beam}^{-1}$. The synthesised beam is 4.3×4.2 arcsec 2 (FWHM) with a position angle of 77° . Bottom: The deepest 610-MHz image obtained to date, covering the same region and with the same linear grey-scale as the VLA image on top. The brightness scale of the image has been multiplied by 0.56 ($= [1400/610]^\alpha$, where $\alpha = -0.7$) in order to visually compare it with the 1.4-GHz map. The restoring beam measures 7.1×6.5 arcsec 2 (FWHM) with a position angle of 70° .

the gain drops to 30 per cent, i.e. at a distance of ~ 28 arcmin from the pointing centre. This final image has a noise level in the central ~ 100 arcmin 2 of $14.7 \mu\text{Jy beam}^{-1}$, the deepest map so far reported at 610 MHz, despite the modest integration time (16 hr on sky for each pointing).

Based on the brightest pixel in the mosaic, $0.032 \text{ Jy beam}^{-1}$, we reach a *dynamic range* between $\sim 2,200 : 1$ and $900 : 1$ considering the central and local r.m.s. noise, respectively. Our images, however, may be long way from being limited by dynamic range. Garn et al. (2008b) reaches $\sim 9,000:1$ and it appears likely that we could push down to the confusion limit in the observations discussed in this paper.

2.2 VLA

New and archival data were obtained in the same three positions using the National Radio Astronomy Observatory's (NRAO²) VLA, largely in its B configuration. At 1400 MHz this yielded images (primary beam FWHM ~ 32 arcmin) well matched to the resolution of GMRT. We tapered our A- and B-configuration data in the LOCKMAN-E field (Ivison et al. 2002) to yield images with a near-circular 4.0-arcsec synthesised beam. Using the same techniques outlined earlier, we then combined this central field with images

² NRAO is operated by Associated Universities Inc., under a cooperative agreement with the National Science Foundation.

GMRT pointings			
Field	R.A. (hr:min:sec)	Dec. (deg:min:sec)	r.m.s. ($\mu\text{Jy beam}^{-1}$)
LHEX-4	10:52:56.0	+57:29:06.0	33.7 (USB)
			29.6 (LSB)
LOCKMAN-E	10:51:59.0	+57:21:28.2	26.2 (USB)
			26.0 (LSB)
LOCK-3	10:51:02.0	+57:13:50.4	24.5 (USB)
			23.7 (LSB)

VLA pointings			
Field	R.A. (hr:min:sec)	Dec. (deg:min:sec)	r.m.s. ($\mu\text{Jy beam}^{-1}$)
LHEX-4	10:52:56.0	+57:29:06.0	7.2
LOCKMAN-E	10:52:08.8	+57:21:33.8	7.6
LOCK-3	10:51:02.0	+57:13:50.4	11.0

Table 1. The GMRT and VLA pointings used in this work. USB and LSB correspond to the upper and lower side bands, respectively.

made using pure B-configuration data in the two other pointings: the designated LOCK-3, 11 arcmin to the south west, for which we obtained 17 hr of data in 2005 March (Ivison et al. 2007); plus archival data for LHEX4, 11 arcmin to the north east of LOCKMAN-E, which comprises 31 hr of integration (see Table 1). The final mosaic-image has an r.m.s. in the central 100 arcmin² of 6.0 $\mu\text{Jy beam}^{-1}$, and a resolution of 4.3 \times 4.2 arcsec² (FWHM) at position angle of 77°.

3 CATALOGUES

Initially, we extracted sources down to a peak-to-local-noise ratio = 3 (hereafter PNR), in order to identify all possible faint and/or extended emission. The sources included in the final catalogues were selected to have PNR ≥ 5 .

3.1 Initial source extraction

Sources were extracted from the final FLATNed mosaics (images of Stokes I), down to a 3- σ (hereafter σ refers to the local noise) peak level, using the *AIPS* routine, SAD (CPARM = 500, 100, 50, 10, 6, 4, 3, 2.5; DPARM(1)=3; DPARM(2)=[15 μJy for GMRT; 7 μJy for VLA]; ICUT = 0.1; GAIN = 1). To provide a reliable noise-based extraction criterion, a noise map was generated from the Stokes I image using RMSD (IMSIZE=71,-1; OPTYPE='HIST'). This noise map was introduced as a secondary image for SAD (DPARM(9) = 3), which ensured reliable source extraction around bright sources and near the map edges (see §7.1). The increasing uncertainties in the SAD-Gaussian fits toward faint PNRs may result in sources having smaller areas than the beamsize (see the smallest CPARM parameter). We use a threshold in peak flux density instead of a threshold in integrated flux because peak flux density is a linearly independent variable in the SAD fitting procedure (actually, in JMFIT), whereas integrated flux density is a product of peak flux and source area. This translates into cleaner and more complete selection criteria. Note, however, that evidences for an anticorrelation between peak fluxes and source area have been found by Condon (1997) in images with uncorrelated noise. Condon shows that this effect disappear when the noise is correlated at similar scales than the synthesised beam. Given by the convolution to a common beamsize made before using FLATN, we expect no anticorrelation in the Gaussian fit parameters.

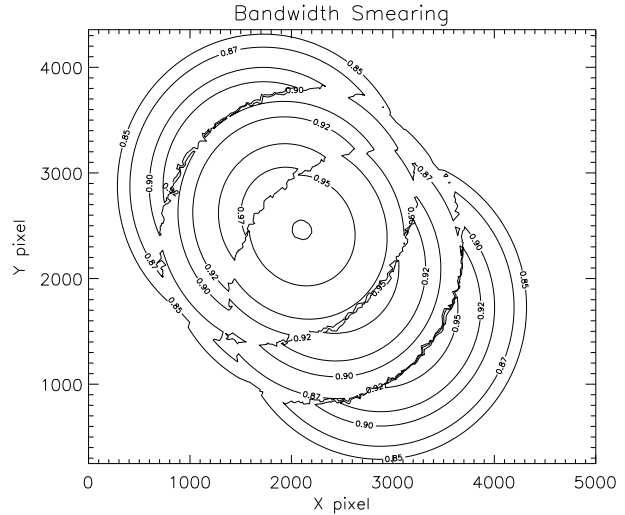


Figure 2. Contour plot for the expected point-source bandwidth-smearing in the 1.4-GHz mosaic (see Eq. 2). Contours are plotted at: 0.85, 0.87, 0.90, 0.92, 0.95 and 0.97. Note that the smallest corrections do not occur exclusively at the image centre.

3.2 Instrumental effects

Four important instrumental effects must be taken into consideration.

3.2.1 Bandwidth smearing

Bandwidth smearing is inevitable when using channels with finite bandwidth. This affects the peak flux densities of sources, but not their integrated fluxes. We have estimated this bias through knowledge of the distance between each source and the different phase centres and use a theoretical correction given by:

$$\frac{I}{I_0} = \frac{1}{\sqrt{1 + \beta^2}} \quad \text{where} \quad \beta = \frac{\Delta\nu}{\nu} \frac{\theta}{\theta_{\text{syn}}} \quad (1)$$

which is valid for point sources, and assumes a Gaussian bandpass and circular tapering in the uv plane (Taylor et al. 1999). I and I_0 are the observed and intrinsic peak brightness, $\Delta\nu$ is the channel bandwidth, ν is the frequency of the bandpass centre, θ_{syn} is the synthesised beamwidth and θ is the distance between the source and the phase centre. This estimation is in agreement with the JM-FIT correction when BWSMEAR is set to the channel bandwidth divided by the center frequency.

In overlapping regions we have averaged the correction by using a minimum variance weighting scheme (see Fig. 2),

$$\left\langle \frac{I}{I_0} \right\rangle = \frac{\sum_i \frac{I_i/I_0}{\text{r.m.s.}_i^2}}{\sum_i \frac{1}{\text{r.m.s.}_i^2}}, \quad (2)$$

which takes into account the noise for each pointing before primary beam correction. This bias was found to be important in the VLA image and not always negligible for the GMRT data. The maximum correction factor was $I/I_0 \approx 0.84$ and $I/I_0 \approx 0.94$ for the VLA and GMRT mosaics, respectively. For example, Fig. 2 shows the bandwidth smearing expected in the VLA mosaic. Note this smearing can be used to correct the peak fluxes in the final cata-

logues (see column 5 in Table 3 and 4), but the selection criterion remained unaffected since it was based on the observed peak values (uncorrected surface brightness, in Jy beam $^{-1}$).

3.2.2 3-D smearing

The general response equation for a two-element interferometer is usually approximated to a 2-D Fourier transform due to the simplicity of the inversion problem. Nevertheless, this is only valid for co-planar baselines (where the w axis lies in the direction of the celestial pole) and for sufficiently small fields of view (Taylor et al. 1999). At low frequencies, the primary beam is large so this approximation becomes inefficient and a formal 3-D Fourier transform is required. A smearing effect is expected from the rotation of the tangential plane with respect to the celestial sphere when the separation between these two is large.

We can estimate the effect of 3-D smearing in our images. For each VLA and GMRT pointing image, we have diameters of ~ 45 and ~ 57 arcmin, respectively, spanned by seven facets. The maximum separation between the tangent plane and the celestial sphere is given by $\Delta = 1 - \cos \phi$, where ϕ is half the subtended angle of each facet (~ 6.4 and ~ 8.1 arcmin, respectively). In our images the maximum separation between each tangent facet and the celestial sphere is ~ 0.09 arcsec at 1.4 GHz and ~ 0.14 arcsec at 610 MHz. In both cases, this separation is equivalent to approximately 2 per cent of the synthesised beamwidth. We consider this bias negligible and no correction to the observed data was made to correct for 3-D smearing.

3.2.3 Time-delay smearing

This smearing is due to the rotation of celestial sources with respect to the phase tracking centre during the integration time, i.e. longer sampling times lead to more blurred images.

In our observations we used 16- and 5-s integration times to collect data from the GMRT and VLA, respectively. Considering theoretical assumptions (again, see Taylor et al. 1999), we find that the maximum loss in peak intensity (expected at the edge of the field of view) is $\lesssim 2$ per cent for GMRT and $\lesssim 0.3$ per cent for the VLA. Consequently, we do not implement any correction to the data for time-delay smearing.

3.2.4 Primary beam attenuation

Primary beam attenuation is the intrinsic loss in gain as a function of distance from the pointing centre due to the antenna response. VLA images were corrected using the default 10th order fit to the beam response at 1.4 GHz, described in *AIPS* (EXPLAIN PBPARM). For the GMRT images we used the 8th order polynomial fit reported by N. G. Kantharia³.

Based on a GMRT mosaic composed of 7 pointings, Garn et al. (2007) reported the primary beam centre was affected by an offset with respect to the phase centre – these two are usually coincident. They revealed a systematic difference between the apparent brightness of sources observed by adjacent pointings, and solved this problem by using a common offset of ~ 2.5 arcmin for the primary beam corrections.

In order to tackle the offset, first we checked that the images created by the upper and lower sidebands (IFs – LSB and USB)

³ www.ncra.tifr.res.in/~ngk/primarybeam/beam.html

from each of our three pointings are giving consistent results for the source estimations. We do not find deviations besides of typical differences in flux calibration of $\lesssim 5$ per cent. Based on these results the IFs were combined in the image plane.

To investigate this thorny issue we define – in overlapping regions – ϕ as the spherical angle formed by the source, the middle distance between two pointings and the northerly direction. Flux ratios are sensitive to pointing variations as a function of ϕ , as shown in Fig. 3. These diagrams can be used to prove if the primary beam is really offset with respect to the phase centre.

In Fig. 3 we plot ϕ as a function of the gain factors $(I_{(1)} - I_{(2)})/(I_{(1)} + I_{(2)})$ and $(S_{(1)} - S_{(2)})/(S_{(1)} + S_{(2)})$, where I is the peak intensity value corrected for bandwidth smearing and S is the integrated flux density (the subindexes (1) and (2) show the pointings being compared). This estimate is based on single sources detected at $\text{PNR} > 25$, and shows no substantial evidence for a primary beam offset. In these plots, the signature expected for a primary beam offset is a sinusoidal data distribution. To measure this effect we use a sinusoidal χ^2 fit, see dashed lines in Fig. 3, to provide the *direction* of the offset via the phase of the fit as well as the amplitude of the offset.

Based on this method to tackle the pointing offset, we find that the use of peak flux values instead of integrated flux densities can result in an *apparent* pointing offset, mostly because of the χ^2 fits obtained for the most widely separated pointings (3–1; bottom in Fig. 3). Smearing effects may thus simulate the behaviour expected for a primary beam offset when I values are used. Since we have accounted for bandwidth smearing, these fits (if robust) suggest smearing is more prevalent than expected. This could be due to inadequate bandpass calibration, but the cause is fundamentally unknown. Since integrated flux densities (S) are not affected by smearing effects, they should provide an unbiased estimation for a primary beam offset. We show in the right-hand panels of Fig. 3, that ϕ does not show compelling signatures for primary beam offsets.

We ran simulations in order to test the reality of the small amplitudes seen in the χ^2 fits, applying different primary beam corrections in the directions indicated by the fits, with the idea of minimising the fitted amplitudes. We found that the offsets required to remove the pointing offsets were $\lesssim 1$ arcmin, with different directions for all the pointings. This contradicts the single offset of ~ 2.5 arcmin, in a common direction, used by Garn et al. (2007).

Due to the lack of evidence for a significant and consistent pointing shift, we decided not to apply any primary beam offset to our data.

3.3 Multiple sources

The definition and identification of multiple systems is a common problem in radio astronomy, i.e. how many fitted Gaussian peaks in the image are related to a single galaxy? This is especially difficult for deep radio observations where extremely deep optical imaging is required to identify the host galaxy. We can look at the image to find obvious double-sided jets from bright, extended radio galaxies (FR II), but this becomes more difficult at faint flux levels for all angular scales, for obvious reasons.

The classification of multiple systems is also highly resolution-dependent. A source adequately described by a single Gaussian at 610 MHz may require more than one component in the higher resolution 1.4 GHz data, confusing catalogues, number counts, and the study of spectral indices. Later, we explicitly refer to 610-MHz- or 1.4-GHz-selected samples to avoid confusion.

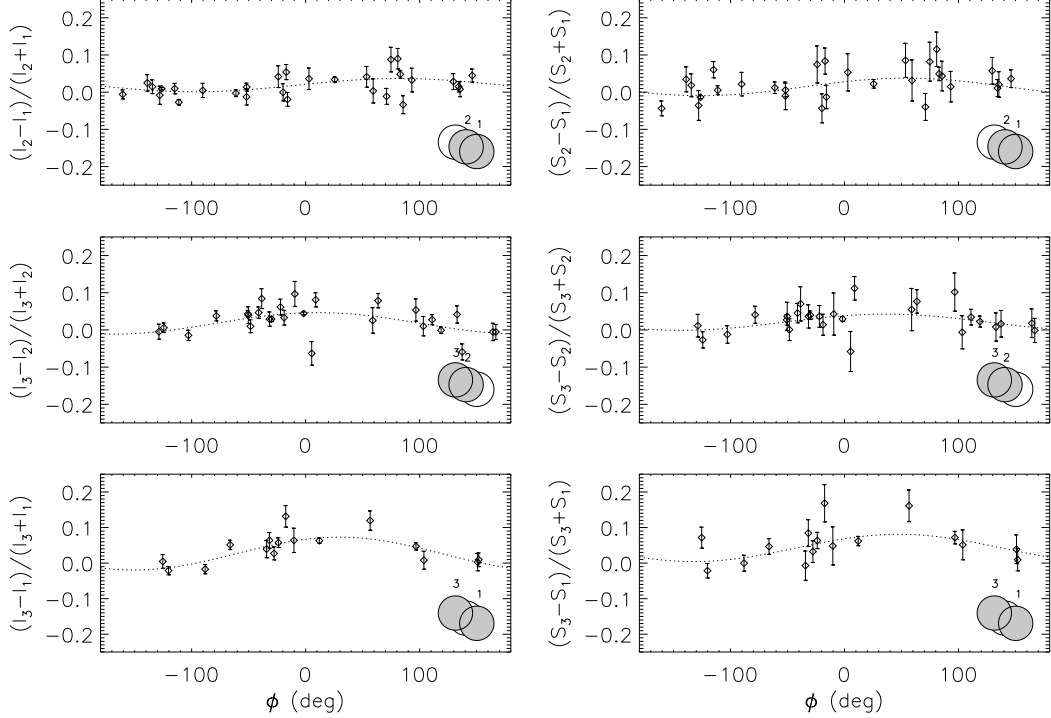


Figure 3. These figures compare source estimates from different pointings in overlapping regions. The y -axis shows the variation in peak brightness corrected by bandwidth smearing (I – left) and integrated flux densities (S – right), for all sources detected with $\text{PNR} > 25$. Subindexes show the pointings being compared (see the bottom-right sketches). The x -axis is the angle ϕ defined in spherical coordinates by the source position, the middle distance between the two pointings and the northerly direction. Dashed lines are sinusoidal χ^2 fits that can provide the direction and amplitude of a primary beam offset with respect to the phase centre.

In order to identify and classify the sources, we filtered the initial 3σ SAD catalogue, excluding all those fits with peak values below $4\times$ the local noise. Then we identified all those detections having close neighbours (with a $\text{PNR} > 4$) based on a simple criterion: if the distance between two Gaussians is lower than $1.2\times$ the sum of their measured FWHMs in the direction defined by the angle they form in the sky (see Fig. 4), then these detections are excluded from the so-called “single-source” sample. We have thus applied a “friend-of-a-friend” technique, using an elliptical (direction-dependent) search radius – an efficient classification method. All these sources have been treated independently in order to check their reliability. Only a small minority of them have been considered as single emitters with more than one Gaussian component. In Table 2 we describe the source classifications. This identification is not restricted in flux density (e.g. Ciliegi et al. 1999; Seymour et al. 2004; Biggs & Ivison 2006) because some sources display diffuse emission, or have fainter components superimposed. The classification is presented in Tables 3 and 4, and is recommended to bear in mind when cross-matching the catalogues.

TVSTAT was used to determine the flux densities of extended sources (usually sources with more than three Gaussian components – see Table 2). This gives a more accurate estimate for complex systems than summing the various Gaussians. A final inspection, by eye, checked the reliability of the components in extended sources (including distant radio lobes in some cases), sources showing side-lobe patterns and sources with diffuse emission not included by the Gaussian fits. For all extended sources, errors in peak and flux density are assumed to be 5 per cent of the value reported by TVSTAT.

Two other important source parameters are the observed an-

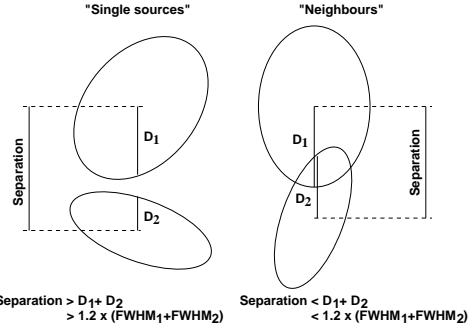


Figure 4. A simple sketch for the selection criteria used to identify sources with close neighbours. If the source in the right were considered to be a double, then it would have an observed angular size given by ‘separation + $(D_1 + D_2)/1.2$ ’ (where D_j are 1.2 times the FWHM in the direction to the neighbour source), and a position angle of 0 deg.

gular size and the orientation of the sources. We have measured the observed angular size as follows. For multiple systems, it corresponds to the separation of the furthest components, plus the measured FWHM of the components in the direction defined by the angle they form on the sky (the ‘position angle’). For single sources, it is equivalent to twice the maximum FWHM. The observed angular size parameter and the phase angle are presented in Tables 3 and 4.

Table 3. A small sample of the sources found in the Lockman Hole field at 610 MHz using the GMRT. Source extraction is based on peak brightness $> 5 \times$ the local r.m.s. and integrated flux density $> 3 \times$ the local r.m.s. criteria. *Columns:* (1) standard source name; (2) right ascension; (3) declination. We note in §3.5 there is an astrometric offset between the VLA with respect to the GMRT sources, $\Delta\text{R.A.} = -0.60 \pm 0.03$ and $\Delta\text{Dec.} = 0.40 \pm 0.03$ arcsec (mean offset in R.A. and Dec., respectively). For double and triple systems the position is given by the brightest component. For extended sources it is given by the most central component; (4) peak flux to local noise ratio; (5) bandwidth smearing correction (§3.2.1); (6) observed maximum angular size (§3.3). These values are not deconvolved source sizes but those fitted from the observed mosaic. For single sources, this value corresponds to twice the maximum FWHM. For multiple sources, it is given by the distance between the furthest components plus the FWHMs of each of them, in the direction they define in the sky; (7) The orientation angle (position angle) of the source with respect to North; (8) integrated flux density and estimated errors from SAD; (9) classification of the source. S = single, D = double (d1 & d2 as components), T = triple (t1, t2 & t3 as components) and M = extended (Table 2). The upper index ($\times 2$) indicates sources extracted from the convolved, $\text{Area}_{\text{beam}} \times \sqrt{2}$, image (§3.4); (10) the radio spectral index between 610 MHz and 1.4 GHz, including the 68.3 per cent confidence range (based on the SAD flux density errors) and upper limits. ‘-’ = outside cross-matching region, ‘!’ = unreliable spectral index; (11) Special flags in spectral indexes: 1 – upper limit, 2 – source which has split the counterpart’s flux density in a relative contribution, 3 – estimation which has used the original SAD extraction before multiple classification, 4 – cross-matched sources separated by a distance > 3 arcsec, 5 – counterparts having a fitted area ratio twice bigger than the expected from point sources ($A_{\text{source}}^{\text{610MHz}} / A_{\text{source}}^{\text{1.4GHz}} > 2 \times A_{\text{beam}}^{\text{610MHz}} / A_{\text{beam}}^{\text{1.4GHz}}$), 6 – estimation based on a cross-match involving more than one counterpart, 7 – spectral index affected by close companion, and 8 – source affected by overlapping facets in the 3-D imaging approach. A complete version of this table is available as Supplementary Material through the on-line version of this paper.

IAU name (1)	Position at 610 MHz hr:min:sec (2)	Position at 610 MHz (J2000) deg:min:sec (3)	PNR (4)	BWSC (5)	Max. size (arcsec) (6)	Position angle (deg) (7)	Flux density (μJy) (8)	Class (9)	$\alpha_{\text{610MHz}}^{\text{610MHz}}$ (10)	α flags (11)
GMRTLHJ105133.4+571459	10:51:33.42	+57:14:59.9	7	0.99	14.3	56	105 \pm 25	S	-0.55 $^{+0.38}_{-0.33}$	
GMRTLHJ105133.6+571308	10:51:33.59	+57:13:08.8	9	0.99	19.1	97	188 \pm 29	S	-1.05 $^{+0.26}_{-0.24}$	
GMRTLHJ105133.6+565039	10:51:33.64	+56:50:39.1	5	0.96	17.8	89	185 \pm 59	S	-	-
GMRTLHJ105134.0+570552	10:51:33.96	+57:05:52.4	8	0.98	14.6	83	116 \pm 25	S	-0.07 $^{+0.36}_{-0.32}$	
GMRTLHJ105134.0+573729	10:51:34.02	+57:37:29.2	11	0.97	15.8	71	242 \pm 35	S	-0.97 $^{+0.26}_{-0.26}$	
GMRTLHJ105134.3+570922	10:51:34.31	+57:09:22.6	7	0.99	13.9	65	177 \pm 45	S	0.81 $^{+0.37}_{-0.39}$	
GMRTLHJ105134.5+573359	10:51:34.46	+57:33:59.4	10	0.98	13.6	67	195 \pm 34	S	-0.52 $^{+0.29}_{-0.26}$	
GMRTLHJ105134.5+573218	10:51:34.53	+57:32:18.2	8	0.98	15.4	178	181 \pm 36	S	-1.46 $^{+0.37}_{-0.36}$	
GMRTLHJ105134.6+574153	10:51:34.65	+57:41:53.3	5	0.96	16.1	0	168 \pm 46	S	< -0.42	1
GMRTLHJ105134.8+571801	10:51:34.81	+57:18:01.6	7	0.99	17.5	65	134 \pm 27	S	-1.23 $^{+0.38}_{-0.38}$	
GMRTLHJ105135.0+564615	10:51:35.02	+56:46:15.7	7	0.94	16.1	51	325 \pm 86	S	-	-
GMRTLHJ105135.2+570133	10:51:35.19	+57:01:33.9	10	0.98	17.4	15	234 \pm 36	SE	-0.80 $^{+0.33}_{-0.36}$	
GMRTLHJ105135.3+570122	10:51:35.27	+57:01:22.4	9	0.98	17.0	81	225 \pm 36	SE	< -0.71	1
GMRTLHJ105135.6+572738	10:51:35.60	+57:27:38.9	23	0.99	14.0	64	324 \pm 24	S	-0.69 $^{+0.12}_{-0.11}$	
GMRTLHJ105135.6+570041	10:51:35.61	+57:00:41.5	6	0.98	19.4	176	215 \pm 49	S	< -0.45	1
GMRTLHJ105135.8+571344	10:51:35.84	+57:13:45.0	6	0.99	22.6	47	145 \pm 32	S	-1.26 $^{+0.45}_{-0.45}$	
GMRTLHJ105135.9+573728	10:51:35.92	+57:37:28.1	6	0.97	13.5	7	92 \pm 28	S	-0.35 $^{+0.50}_{-0.43}$	
GMRTLHJ105136.0+573424	10:51:36.05	+57:34:24.7	5	0.98	13.3	7	73 \pm 26	S	< -0.31	1
GMRTLHJ105136.1+574410	10:51:36.06	+57:44:10.0	5	0.97	17.8	37	130 \pm 38	S	< -0.28	1
GMRTLHJ105136.2+572959	10:51:36.20	+57:29:59.1	27	0.99	15.3	72	605 \pm 36	S	-0.83 $^{+0.09}_{-0.09}$	
GMRTLHJ105136.3+570651	10:51:36.28	+57:06:51.2	9	0.98	13.2	41	132 \pm 25	SD	-0.96 $^{+0.39}_{-0.42}$	
GMRTLHJ104809.1+570414	10:48:09.07	+57:04:14.9	5	0.95	30.0	33	330 \pm 90	S($\times 2$)	-	-

Table 4. The 1.4-GHz catalogue. See Table 3 for details.

IAU name (1)	Position at 1.4 GHz hr:min:sec (2)	Position at 1.4 GHz (J2000) deg:min:sec (3)	PNR (4)	BWSC (5)	Max. size (arcsec) (6)	Position angle (deg) (7)	Flux density (μJy) (8)	Class (9)	$\alpha_{\text{610MHz}}^{\text{610MHz}}$ (10)	α flags (11)
VLAHLJ105211.4+571551	10:52:11.44	+57:15:51.7	5	0.95	8.3	178	28 \pm 9	SD	-0.53 $^{+0.40}_{-0.50}$!	2
VLAHLJ105211.5+573953	10:52:11.48	+57:39:53.2	21	0.90	9.2	46	193 \pm 17	S	0.11 $^{+0.28}_{-0.24}$	
VLAHLJ105211.8+573510	10:52:11.82	+57:35:10.2	12	0.94	7.1	37	53 \pm 8	SD	-1.55 $^{+0.35}_{-0.32}$!	5
VLAHLJ105211.9+570540	10:52:11.86	+57:05:40.5	7	0.91	9.9	161	58 \pm 16	S	-0.22 $^{+0.50}_{-0.49}$	
VLAHLJ105212.0+572321	10:52:12.04	+57:23:21.6	6	0.97	7.4	146	24 \pm 7	S	-1.48 $^{+0.54}_{-0.54}$	
VLAHLJ105212.1+573454	10:52:12.08	+57:34:54.6	9	0.95	8.0	161	46 \pm 10	S	> -0.98	1
VLAHLJ105212.1+572621	10:52:12.11	+57:26:21.4	10	0.97	10.2	136	64 \pm 10	S	-0.38 $^{+0.52}_{-0.41}$	
VLAHLJ105212.2+571525	10:52:12.16	+57:15:25.4	9	0.94	10.4	73	68 \pm 12	S	-1.00 $^{+0.28}_{-0.28}$	
VLAHLJ105212.3+571549	10:52:12.27	+57:15:49.5	19	0.95	8.0	90	84 \pm 8	SD	-0.53 $^{+0.22}_{-0.20}$!	2
VLAHLJ105212.5+572453	10:52:12.49	+57:24:53.1	48	0.97	9.2	97	278 \pm 10	S	-0.62 $^{+0.10}_{-0.09}$	
VLAHLJ105212.6+570641	10:52:12.63	+57:06:41.3	6	0.92	10.2	32	56 \pm 17	S	-1.61 $^{+0.41}_{-0.48}$	
VLAHLJ105213.3+572650	10:52:13.29	+57:26:50.6	12	0.97	9.3	156	71 \pm 9	S	> -0.30	1
VLAHLJ105213.4+571605	10:52:13.38	+57:16:05.3	52	0.95	8.8	59	301 \pm 10	S	-0.77 $^{+0.06}_{-0.06}$	
VLAHLJ105213.4+572600	10:52:13.44	+57:26:00.2	10	0.97	7.8	161	45 \pm 8	S	-0.43 $^{+0.50}_{-0.41}$	
VLAHLJ105213.6+574436	10:52:13.64	+57:44:36.0	6	0.89	7.8	166	64 \pm 21	S	> -0.93	1
VLAHLJ105213.8+571338	10:52:13.76	+57:13:38.9	13	0.93	9.2	5	89 \pm 11	SD	-0.82 $^{+0.24}_{-0.23}$!	2
VLAHLJ105213.9+573935	10:52:13.89	+57:39:35.9	9	0.90	7.4	124	54 \pm 12	S	> -0.95	1
VLAHLJ105214.0+571841	10:52:14.04	+57:18:42.0	6	0.96	11.9	107	44 \pm 11	S	-1.32 $^{+0.42}_{-0.44}$	
VLAHLJ105214.2+573140	10:52:14.18	+57:31:40.9	7	0.97	14.1	38	91 \pm 17	S	> -0.62	1
VLAHLJ105214.2+573328	10:52:14.21	+57:33:28.2	7	0.96	11.9	35	85 \pm 17	S	-0.91 $^{+0.41}_{-0.37}$	
VLAHLJ105214.6+571335	10:52:14.60	+57:13:35.9	5	0.93	7.9	62	24 \pm 8	SD	-0.82 $^{+0.42}_{-0.54}$!	2
VLAHLJ104914.4+570210	10:49:14.41	+57:02:10.4	5	0.86	14.2	145	231 \pm 69	S($\times 2$)	-0.56 $^{+0.36}_{-0.44}$	

Class	Description
S	Single Gaussian source without close neighbours
SD	Single Gaussian source with one close neighbour
ST	Single Gaussian source with two close neighbours
SE	Single Gaussian source with multiple close neighbours
D	Double Gaussian source without close neighbours
DT	Double Gaussian source with one close neighbour
T	Triple Gaussian source without close neighbours
M	Extended source composed of more than three Gaussians

Table 2. Source classifications for the radio catalogues presented in Tables 3 and 4. By ‘neighbours’ we mean sources extracted by SAD with PNR > 4, using the criteria shown in Fig. 4.

3.4 Source catalogues

Various clean-up processes were applied to the initial catalogues produced by SAD (see §3.1). First, we eliminated those sources lying closer than 30 pixels (24 and 37.5 arcsec at 1.4 GHz and 610 MHz) from the image border, where the noise is considerably higher, and removed sources forming part of multiple structures that have been considered as single emitters. The final catalogues comprise sources with PNR > 5 (uncorrected by bandwidth smearing) and integrated fluxes in excess of $3 \times$ the local r.m.s. (this avoids a small number of sources with extremely small sizes).

Lastly, we ran both source extractions again using $\sqrt{2} \times \text{Area}_{\text{beam}}$ convolved images to include extended emission missed by the first selection process. We found 16 and 43 new sources in the GMRT and VLA mosaics, respectively.

Final catalogues are presented in Tables 3 and 4. We have identified a total number of 1,587 and 1,452 sources with $\text{PNR} \geq 5\sigma$ at 610 MHz and 1.4 GHz, respectively.

3.5 Astrometric precision

We plot in Fig. 5 the offsets of the VLA sources with respect to the GMRT positions, using only single sources (§3.3). The offset distribution is approximately Gaussian with a mean of $\Delta\text{R.A.} = -0.60 \pm 0.03$ and $\Delta\text{Dec.} = 0.40 \pm 0.03$ arcsec. These mean offsets, ~ 0.5 arcsec, are observed at all flux levels, and their origin is unknown. Garn et al. (2007) found an incorrect time stamp in the GMRT data, resulting in a rotation of the positions near the edge of each pointing. This problem was corrected during the reduction of our data and is not responsible for the observed offsets, which may instead relate to VLA correlator issues which have only recently come to light (Morrison et al. 2009, in preparation), or be due to a different position for the phase calibrators used at the different frequencies.

An external reference was used to test the 610-MHz astrometry – recent work by Garn et al. (2008b), which includes a 610-MHz observation in the Lockman Hole. We find about 90 common sources (see §7.1 for details) with a median offset of $\Delta\text{R.A.} = -0.54 \pm 0.05$ and $\Delta\text{Dec.} = 0.00 \pm 0.04$. These offsets help explain the R.A. offset found in Fig. 5, but not that in Dec.

We have been unable to find a straightforward reason for the observed offsets between the VLA 1.4-GHz and GMRT 610-MHz sources. We have not implemented a positional shift in our catalogues, although we highlight this issue in the table captions.

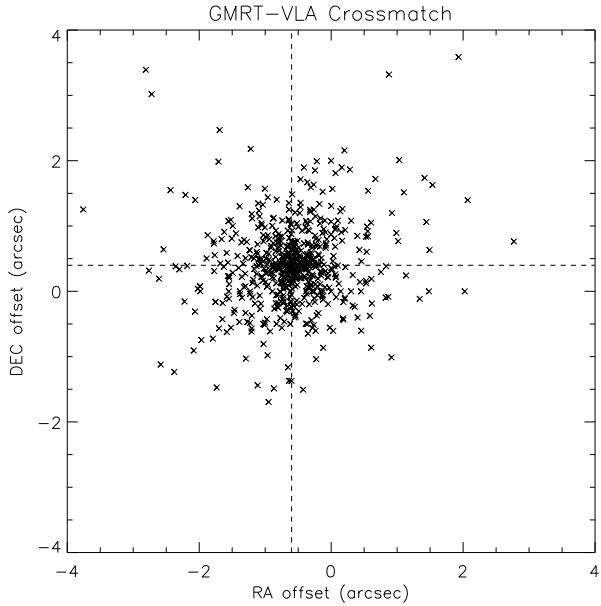


Figure 5. Relative offsets between single sources found at 1.4 GHz with respect to the 610-MHz GMRT positions. Offsets are approximately normally distributed. In R.A. and Dec. we find mean offsets of -0.60 ± 0.03 and 0.40 ± 0.03 arcsec, respectively. *Dashed lines* show the mean offset values.

4 NUMBER COUNTS

We have derived number counts in the Lockman Hole using the catalogues shown in Tables 3 and 4. The differential number counts, dN/dS , were calculated using the observed number of sources per bin of flux density, N , divided by the bin width (ΔS in Jy) and by the effective area (A_{eff} in steradians) available for detection.

$$\frac{dN}{dS} = \frac{N}{A_{\text{eff}} \Delta S} \quad (3)$$

4.1 Effective area

In our catalogues, the selection criteria for radio emitters is determined by the local noise at the position of the source and by the effectiveness of SAD in detecting the sources. In particular, we note the noise across the image has a complicated structure and is correlated on several different scales. In order to find the effective area for source detection as a function of flux density, we modelled 25,000 point sources using the task IMMOD, with peaks from $1\times$ to $500\times$ the central r.m.s. in the mosaic ($\sim 15 \mu\text{Jy beam}^{-1}$ at 610 MHz and $\sim 6 \mu\text{Jy beam}^{-1}$ at 1.4 GHz). We performed the simulations by introducing 500 mock sources into a residual image (without $\geq 5\sigma$ positive or negative sources). We made use of two different (but complementary) residual images obtained from the negative (inverted) and the ‘positive’ (normal) maps. This allowed us to assess flux boosting due to random associations with faint, real sources. We then extracted a catalogue using SAD, with the same criteria as those described in §3. Mock sources were introduced, taking into account bandwidth smearing, with random position angles, located >30 pixels from the image border, none of them overlapping. Bright residuals around powerful radio sources were avoided too – regions in the vicinity of the brightest 20 sources. The process of introducing sources was repeated 50 times.

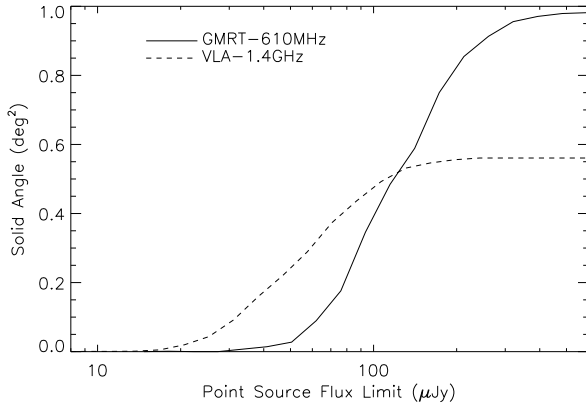


Figure 6. Solid angle versus point-source flux limit. *Solid* and *dashed* lines are based on GMRT and VLA mosaics, covering a total of 3,534 and 2,019 arcmin², respectively.

Since mock sources were introduced randomly in the image, we can assume that the completeness function – the ratio of sources extracted to those injected – as a function of flux density, normalised to the area of the field, provides the effective area, $A_{\text{eff}}(S)$, which includes all possible biases from the SAD extraction and due to the noise structure of the map.

Fig. 6 shows the solid angle versus point-source flux limit used in Eq. (3) to estimate the differential number counts at 610 MHz and 1.4 GHz.

4.2 Resolution bias

In this work, most of the sources lie in the sub-mJy regime and the angular size distribution of the sub-mJy radio population is not well known. Given the low resolution of our GMRT and VLA maps, the vast majority of the sources are point-like ($\lesssim 4$ arcsec), therefore based on our data we are unable to obtain a detailed and self-consistent angular size distribution.

Source catalogues based on a PNR-threshold criterion are biased against extended sources as a function of flux density. In order to estimate the fraction of sources being missed by our threshold criterion, we applied the following treatment.

4.2.1 Area threshold

Number counts are calculated as a function of integrated flux density, while our catalogues are mainly based on a PNR threshold criterion. This restricts the detection of faint radio sources to those with small angular sizes. The resolution bias can be simply estimated using the following equation:

$$\frac{\text{Flux}_{[\text{SAD}]}^{} }{\text{Peak}_{[\text{SAD}]}^{} } = \frac{A_{\text{source}}}{A_{\text{beam}}^{} } = \left(\frac{\pi}{4 \ln 2} \right) \frac{\text{Bmaj}_{[\text{SAD}]}^{} \text{Bmin}_{[\text{SAD}]}^{} }{A_{\text{beam}}^{} } \quad (4)$$

where the [SAD] index indicate values from one single Gaussian from the SAD output fit; integrated ‘Flux’ is given in Jy, ‘Peak’ flux in Jy beam⁻¹, Bmaj and Bmin are the fitted major and minor FWHMs in arcsec (not the deconvolved source size), and the synthesised beam area, $A_{\text{beam}} = \left(\frac{\pi}{4 \ln 2} \right) \text{Bmaj}^{\text{beam}} \text{Bmin}^{\text{beam}} \text{arcsec}^2$.

Eq. (4) implies that for our PNR threshold, the fitted area of a source as a function of flux density is restricted to:

$$A_{\text{source}} \leq \frac{A_{\text{beam}}}{5 \times \text{r.m.s.}} \text{Flux} \quad (5)$$

In particular, our PNR threshold implies the faintest sources are restricted to be detected with small fitted areas, $A_{\text{source}} \approx A_{\text{beam}}$, or a little smaller than the beam given by the uncertainties in the fit. Note that Eq. (5) applies to sources fitted with a single Gaussian only – this is the case for the vast majority of the sources analysed in this work.

4.2.2 Angular size distribution

Previous studies have shown a decreasing angular size of the radio sources towards faint flux densities. An early study, Windhorst et al. (1990) parameterised the angular size distribution of the radio emitters using the following equation:

$$h(\theta) = \exp[-\ln(2) \times (\theta/\theta_{\text{med}})^{0.62}] \quad (6)$$

where $h(\theta)$ is defined as the cumulative fraction of sources with angular sizes larger than θ (the major FWHM) and $\theta_{\text{med}} = 2 \times S_{1.4\text{GHz}}^{0.3}$ arcsec is the median angular size as a function of flux density (in mJy). This estimate predicts small variations in θ_{med} as a function of radio flux density. Bondi et al. (2003), however, found that the Windhorst et al. distribution yields a considerably higher number of sources with large angular sizes – by almost a factor of two (with $\theta > 4$ arcsec) than the observed in the sub-mJy regime. This translates into an overestimate of the sources expected to be missed in our observations. Bondi et al. (2003) found that the cumulative angular size distribution of sources with $0.4 \leq S_{1.4\text{GHz}} < 1$ mJy (expected to be unbiased for $\theta \lesssim 15$ arcsec sources) is well described by:

$$h(\theta) = \begin{cases} (1.6^\theta)^{-1} & \text{for } \theta \leq 4 \text{ arcsec} \\ \theta^{-1.3} - 0.01 & \text{for } \theta > 4 \text{ arcsec} \end{cases} \quad (7)$$

High-resolution radio observations (Muxlow et al. 2005; Biggs & Ivison 2008), using data from both the Multi-Element Radio-Linked Interferometer Network (MERLIN) and the VLA, have given us an angular size distribution for the sources in the $40 \mu\text{Jy} < S_{1.4\text{GHz}} \lesssim 1$ mJy regime. Almost all the sources are resolved with angular sizes below 4 arcsec, which implies that our observations might be unaffected by resolution bias at μJy flux densities. Nevertheless, Muxlow et al. estimate their sample is 10 per cent incomplete based on previous observations with the Westerbork Synthesis Radio Telescope (WSRT; with a synthesised beam-size of 15 arcsec, FWHM) in the same field, which we use as an upper limit for μJy detections.

We have adopted a cumulative angular size distribution given by Eq. (6) for bright (> 1 mJy) sources, and the average of Eqs (6) and (7) for fainter sources.

4.2.3 Correction factors

In order to relate Eq. (5) to the assumed cumulative angular size distribution, we have considered $\theta = \sqrt{A_{\text{source}}/1.1331/\eta}$, where η is the median ratio between the major and minor FWHM (broadened by smearing effects) of the observed VLA sources, $\eta = 0.80$. Although this is a strong assumption, changing this parameter does not significantly modify our results.

In Fig. 7 we plot the expected missed fractions as a function of

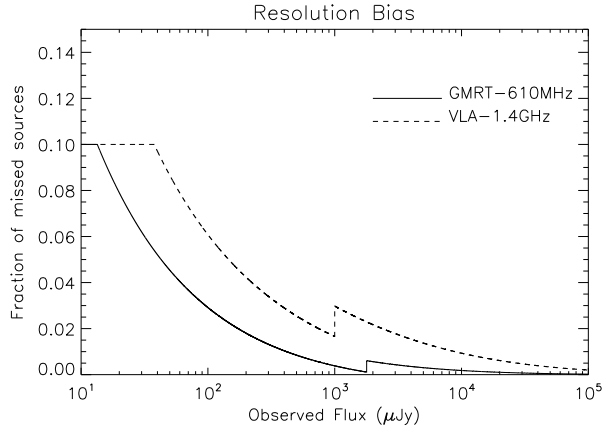


Figure 7. Estimated missed fraction of extended sources as a function of flux density. *Solid* and *dashed* lines are the estimates for the VLA and GMRT detections, respectively. Estimates are based on Eq. (5) and an averaged cumulative size distribution based on Eq. (6) and (7) – see §4.2.1 and §4.2.2. We have assumed a spectral index of $\alpha = -0.7$ for the GMRT predictions.

flux density for both observing frequencies. Note, we have assumed a threshold of 10 per cent incompleteness for our faintest radio flux levels, based on Muxlow et al. (2005).

Since the angular size distribution of the 610-MHz sources is more uncertain than that of the 1.4-GHz sources, we have assumed a radio spectral index of $\alpha = -0.7$ to calculate the missed fraction at 610 MHz.

These correction factors are small due to the relatively poor resolution of our observations. Indeed, this bias is minimised when we include extended sources extracted from the convolved images (§3.4). In particular, at $100 \mu\text{Jy}$ we predict that 3 per cent of GMRT sources and 6 per cent of VLA sources are not selected in our catalogues.

4.3 Differential number counts

The differential number counts from Eq. (3), normalised for an Euclidean Universe, are plotted in Fig. 8. At both frequencies we have used the effective area shown in Fig. 6 and the correction for resolution bias plotted in Fig. 7. The flux density used to multiply the differential number counts is given by the bin centre (in log space), and errors are Poissonian for uncorrected counts, for both the observed and mock sources. Tables 5 and 6 present the counts.

We observe a flattening in the Euclidean differential number counts towards sub-mJy flux densities at both 610 MHz and 1.4 GHz (Fig. 8). We find evidence for a second peak in number counts at $\sim 80 \mu\text{Jy}$ and $\sim 200 \mu\text{Jy}$ for the VLA and GMRT counts, respectively. These provide constraints on the contribution of *IRAS*-like sources to the sub-mJy radio fluxes, based on population synthesis models (Hopkins et al. 2000). The appearance of these features at sub-mJy radio fluxes is traditionally explained as a transition from a dominant bright radio-loud AGN population to a star-forming and radio-quiet AGN populations (Windhorst et al. 1985; Simpson et al. 2006; Condon 2007).

In this work we extend the number counts down to very faint 610-MHz flux densities whilst maintaining complete agreement with previous studies at higher flux levels. Our results at 1.4 GHz are in good agreement with previous observations at $\gtrsim 200 \mu\text{Jy}$ using the VLA’s B configuration (Bondi et al. 2003; Seymour et al.

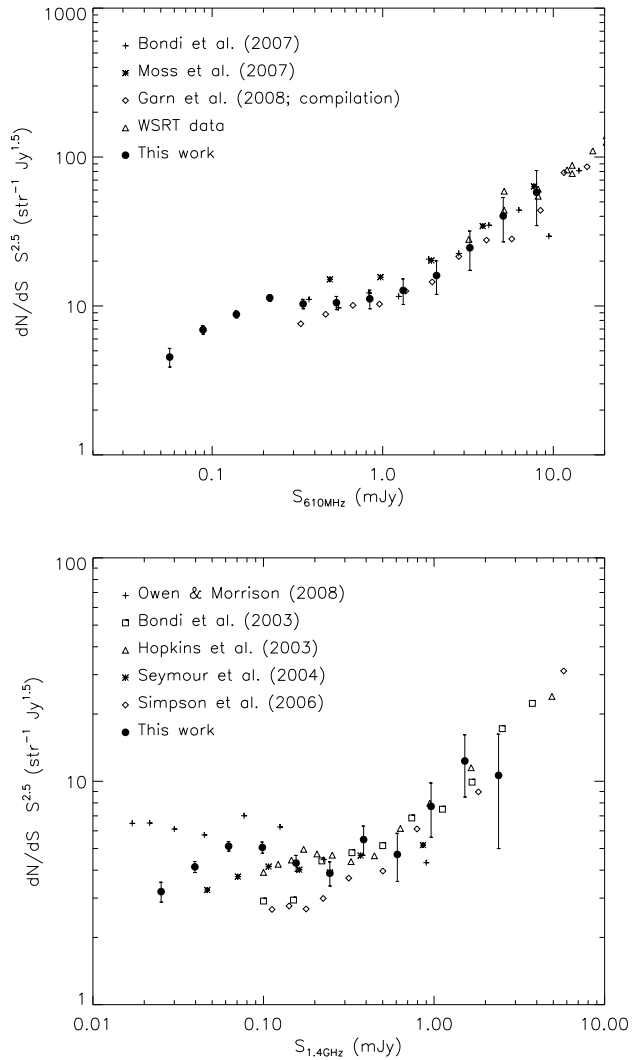


Figure 8. Differential source counts as a function of flux density in the Lockman Hole at 610 MHz (*top*) and 1.4 GHz (*bottom*), normalised by the value expected in a static Euclidean Universe. Errors are assumed to be Poissonian (Gehrels 1986) and are combined in quadrature for the observed number of sources in the bin and the mock source simulations described in §4.1. At 610 MHz, we plot data from previous studies: the VLA-VIRMOS Deep Field (Bondi et al. 2007), the 1^h *XMM-Newton/Chandra* Survey (Moss et al. 2007), a compilation from Garn et al. (2008b) which includes data from the ELAIS N1, Lockman Hole and *Spitzer* First-Look Survey fields and counts obtained using the WSRT (Valentijn et al. 1977; Katgert 1979; Valentijn 1980; Katgert-Merkelijn et al. 1985). We also show previous 1.4-GHz counts, based on studies using the VLA and using the Australia Telescope Compact Array: The Deep Swire Field (Owen & Morrison 2008), the Phoenix Deep Survey (Hopkins et al. 2003), VLA-VIRMOS Deep Field (Bondi et al. 2003), the 13^h *XMM-Newton/ROSAT* Deep X-ray Survey (Seymour et al. 2004) and the Subaru/*XMM-Newton* Deep Field (Simpson et al. 2006).

2004) and the Australia Telescope Compact Array (Hopkins et al. 2003). At fainter levels, $< 100 \mu\text{Jy}$, our 1.4-GHz counts are a little higher than the majority of previous estimates. This may reflect underestimates of number counts based on shallower images; for example, Owen & Morrison (2008) reported an approximately flat $\log N$ - $\log S$ distribution down to $S_{1.4\text{GHz}} \sim 15 \mu\text{Jy}$, exploit-

Table 5. The 610-MHz radio source counts.

S bin (mJy)	S (mJy)	N	$N/\Delta S/A_{\text{eff}}$ (str $^{-1}$ Jy $^{-1}$)	$dN/dS \times S^{2.5}$ (str $^{-1}$ Jy $^{1.5}$)
0.045 - 0.071	0.056	58	$(1.90 \pm 0.27) \times 10^{11}$	4.54 ± 0.65
0.071 - 0.111	0.088	253	$(9.41 \pm 0.61) \times 10^{10}$	6.92 ± 0.45
0.111 - 0.174	0.139	379	$(3.88 \pm 0.20) \times 10^{10}$	8.79 ± 0.46
0.174 - 0.273	0.218	389	$(1.62 \pm 0.09) \times 10^{10}$	11.35 ± 0.59
0.273 - 0.428	0.341	211	$(4.79 \pm 0.35) \times 10^9$	10.33 ± 0.75
0.428 - 0.671	0.536	114	$(1.58 \pm 0.16) \times 10^9$	10.52 ± 1.07
0.671 - 1.052	0.840	62	$(5.46 \pm 0.78) \times 10^8$	11.17 ± 1.60
1.052 - 1.651	1.318	36	$(2.02 \pm 0.39) \times 10^8$	12.72 ± 2.49
1.651 - 2.590	2.068	23	$(8.24 \pm 2.09) \times 10^7$	16.02 ± 4.07
2.590 - 4.063	3.244	18	$(4.10 \pm 1.21) \times 10^7$	24.60 ± 7.25
4.063 - 6.374	5.089	15	$(2.18 \pm 0.72) \times 10^7$	40.23 ± 13.29
6.374 - 10.000	7.984	11	$(1.02 \pm 0.41) \times 10^7$	57.92 ± 23.26

ing an extremely deep VLA 1.4-GHz image of the 1046+59 field (r.m.s. ~ 3 μ Jy). The decrement of the number of radio sources towards faint flux densities (Fig. 8) is highly dependent on the effective area, A_{eff} , in which detections are possible (Fig. 6). We find A_{eff} always decreases slower in relation to the number of sources in each bin, so underestimating our number counts would require us to have undercorrected for resolution bias. We note, however, that even adopting the Windhorst et al. (1990) size distribution could not increase the number counts to those found by Owen & Morrison.

A large number of faint radio sources was suggested recently by the Absolute Radiometer for Cosmology, Astrophysics and Diffuse Emission (ARCADE 2 – Fixsen et al. 2009) experiment where an excess brightness temperature was found in the 22 MHz–10 GHz range, where the sky is expected to be dominated by synchrotron and free-free emission from extra-galactic sources and the Milky Way. Fixsen et al. (2009) reported seeing approximately $5\times$ the expected contribution from faint radio sources (Gervasi et al. 2008) to the cosmic microwave background, which sets a useful limit for the total number of radio sources.

The origin of the wide scatter in reported 1.4-GHz number counts is controversial. It is possible that for $< 500 \mu$ Jy sources our imaged area is not big enough to average out cosmic structure. For a field subtending an angle of one square degree, the angular diameter distance at redshift unity is only ~ 20 Mpc. We note that Condon (2007) estimated a count fluctuation of only $\sigma = (1.07 \pm 0.26) N^{1/2}$ based on 17 non-overlapping fields in the *Spitzer* First-Look Survey (FLS – Condon et al. 2003), where $N^{1/2}$ is the statistical fluctuation expected without clustering. Based on this, Condon (2007) stated that most of the variance reported in the literature is ‘mundane, not cosmic’, thereby concluding that years of debate have been devoted to differences induced by different instruments and analysis techniques (see §7.2) and possibly – in more candid terms – human error. Biggs & Ivison (2006) came to a similar conclusion, finding around double the source count in the *Hubble* Deep Field North as had been measured by Richards (2000) and tracking the problem to a simple arithmetical error rather than any fundamental problem with the data or their reduction.

Another possible origin for some of the reported scatter may be the use of different VLA configurations for deep survey work, either through problems setting the absolute flux scale, or via inadequate correction for bandwidth smearing. We have separated the A- and B-configuration data centred on our LOCKMAN-E VLA pointing to test if this introduces notable differences. We find a value of $S_A/S_B = 1.03 \pm 0.21$ for the mean and standard deviation of the flux density ratios observed on sources detected in both con-

Table 6. The 1.4-GHz radio source counts.

S bin (mJy)	S (mJy)	N	$N/\Delta S/A_{\text{eff}}$ (str $^{-1}$ Jy $^{-1}$)	$dN/dS \times S^{2.5}$ (str $^{-1}$ Jy $^{1.5}$)
0.020 - 0.032	0.025	95	$(1.01 \pm 0.10) \times 10^{12}$	3.21 ± 0.33
0.032 - 0.050	0.040	284	$(4.19 \pm 0.24) \times 10^{11}$	4.14 ± 0.24
0.050 - 0.078	0.062	388	$(1.66 \pm 0.08) \times 10^{11}$	5.12 ± 0.25
0.078 - 0.124	0.098	303	$(5.25 \pm 0.30) \times 10^{10}$	5.06 ± 0.29
0.124 - 0.195	0.155	158	$(1.43 \pm 0.12) \times 10^{10}$	4.30 ± 0.35
0.195 - 0.308	0.245	76	$(4.13 \pm 0.51) \times 10^9$	3.88 ± 0.48
0.308 - 0.485	0.386	55	$(1.87 \pm 0.28) \times 10^9$	5.48 ± 0.82
0.485 - 0.765	0.609	24	$(5.14 \pm 1.25) \times 10^8$	4.70 ± 1.14
0.765 - 1.206	0.961	20	$(2.70 \pm 0.74) \times 10^8$	7.72 ± 2.11
1.206 - 1.902	1.515	16	$(1.38 \pm 0.43) \times 10^8$	12.33 ± 3.83
1.902 - 3.000	2.389	7	$(3.81 \pm 2.02) \times 10^7$	10.63 ± 5.63

figurations with peak-to-noise ratios greater than 10 (42 sources). We conclude that use of different configurations does not significantly bias estimates of flux densities in our catalogues. The scatter must originate elsewhere, assuming that data have been calibrated carefully, using appropriate *uv* restrictions or calibrator models.

Noise can contaminate the number counts through the inclusion of spurious sources and by boosting intrinsically faint sources to higher flux densities. We have tested the possibility that spurious sources contaminate the samples by implementing an identical source extraction procedure for the inverted (negative) signal map and we are confident that any contamination by spurious sources is below 5 per cent, even in the faintest flux density bins.

5 SPECTRAL INDICES

We have cross-matched (within 7 arcsec) the GMRT and VLA radio catalogues in order to estimate the spectral index of the radio emitters. This measurement yields evidence for the synchrotron mechanism which dominates the observed radiation from the sub-mJy radio population.

In Fig. 9 we show the spectral index between 610 MHz and 1.4 GHz as a function of flux density. We now analyse the spectral indices based independently on GMRT- and VLA-selected samples, where a 610-MHz-selected catalogue naturally tends to prefer the detection of steep-spectrum sources while selection at 1.4 GHz favours flatter spectra.

Since the VLA and GMRT images have different resolutions, special care must be taken when we analyse results based on different frequency-selected samples. The 610-MHz catalogue, from a lower-resolution image, tends to have more counterparts per source than the 1.4-GHz catalogue. This issue confuses the statistical studies of spectral indexes since more unrelated galaxies are summed up or split depending on the sample criterion. For example, given our selection criteria and the resolution difference between the observing frequencies, it is possible that a single source at 610 MHz is related to two single detections at 1.4 GHz. In this case, the spectral index of the GMRT source is calculated using the sum of the flux densities from both VLA sources. For the VLA-selected sources we have divided the flux density at 610 MHz based on the relative contribution from each VLA source (spectral indexes based on split sources are flagged as such). Where there is no clear close counterpart (within 7 arcsec), 5- σ upper/lower limits are calculated using the local r.m.s. (§3.1), weighting by the source to beam area ratio.

Fig. 9 shows the spectral indices for GMRT-selected (*top*) and VLA-selected (*bottom*) samples. Both distributions show a large scatter, casting doubt on previous studies which assume a clean

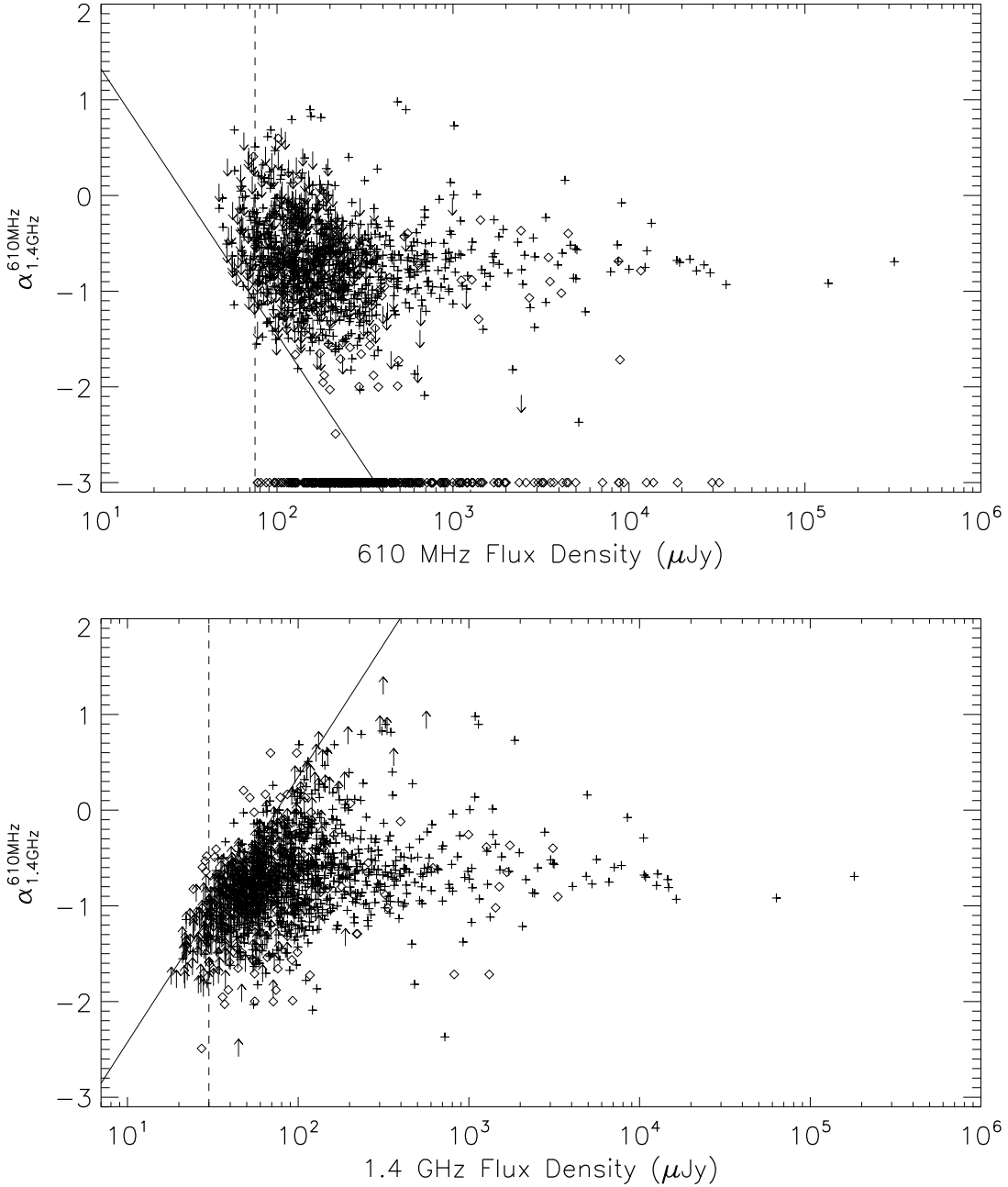


Figure 9. Spectral index, $\alpha_{1.4\text{GHz}}^{610\text{MHz}} = -2.77 \times \log(S_{610\text{MHz}}/S_{1.4\text{GHz}})$, as a function of flux density, based on a 610-MHz-selected sample (top) and a 1.4-GHz-selected sample (bottom). Dashed and solid lines correspond to the primary and secondary point-source flux limit for each survey. Plus symbols represent detections. Arrows represent upper and lower limits for GMRT and VLA sources, respectively. Diamonds represent unreliable spectral indexes – sources that were split, missing fainter components, or large offsets in the cross-match. The data at $\alpha = -3$ are sources outside the overlapping region.

star-forming galaxy population with a single spectral index in the sub-mJy radio regime.

Upper/lower limits dominate at the faintest fluxes, partly due to the difficulty in obtaining counterparts so close to the detection threshold, where the catalogues are incomplete, and partly due to the tendency to detect steeper-spectrum sources at 610 MHz or flatter-spectrum sources at 1.4 GHz. In our work, this bias does not allow the study of spectral index for sources with $S_{1.4\text{GHz}} \lesssim 100 \mu\text{Jy}$. The larger number of lower limits at 1.4 GHz reflects the extra depth of the VLA imaging.

In Table 7 we show the observed statistical results for spectral indices as a function of flux density (parenthesis show mock values – see below). In order to avoid a large fraction of upper limits in these statistical calculations, we have used only $\geq 10\sigma$ (PNR) detections for each of the catalogue-based samples, but down to 5σ for the counterpart. We find no trend in the distribution of spectral indexes toward fainter flux densities in either the GMRT- or the VLA-selected catalogues. Since these two samples tend to select spectra with different spectral indexes, numerical differences of ~ 0.2 in the mean α , and ~ 0.1 in the median, are seen in the esti-

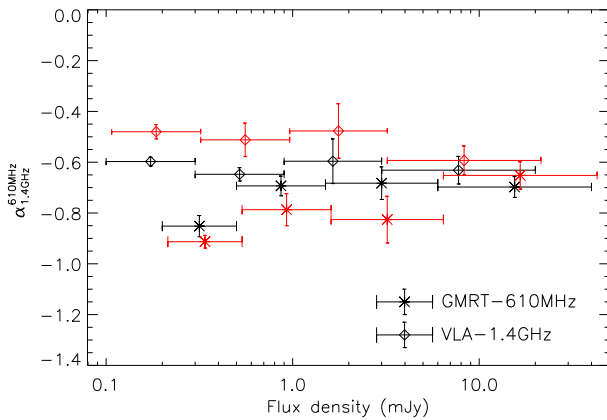


Figure 10. The median-bootstrapped (in black) and the Kaplan-Meier (Feigelson & Nelson 1985) mean (in red) spectral indices as a function of flux density. Data are based on 610-MHz- and 1.4-GHz-selected samples and shown in Table 7. In the image, mean values are slightly shifted in flux density (just for clarity).

mates for similar flux density bins. These results contradict the suggested flattening in spectral index at sub-mJy radio flux densities quoted in previous studies (Bondi et al. 2007; Garn et al. 2008a).

The almost constant mean and median values of α in the sub-mJy regime (certainly between 0.1 – 10 mJy) is a robust result, and suggests the sub-mJy radio population is dominated by optically-thin synchrotron emission from star-forming galaxies and/or from steep-spectrum lobe-dominated FR AGN. We show the trend for the mean and median spectral index as a function of flux density in Fig. 10. The mean (in red) includes upper/lower limits using the Kaplan-Meier product-limit estimator (ASURV – Feigelson & Nelson 1985), and the median (in black) is obtained from detections using a bootstrapping approach. The small variations in these estimates reflect the non-Gaussianity and the large scatter of the distribution, especially for the faintest detections. In particular, the very steep spectral index obtained from the faintest GMRT flux bin contains ~ 20 per cent of upper limits, a result which may be slightly biased toward steeper spectral indexes (see simulations in parenthesis from Table 7).

The scatter of the $\alpha_{1.4GHz}^{610MHz}$ distribution is $\sigma_\alpha \approx 0.4$ in the sub-mJy regime, which suggests the detection of a large variety of populations – probably a substantial number of synchrotron self-absorbed AGN cores (Blundell & Kuncic 2007; Snellen et al. 2000) and high-redshift ultra-steep-spectrum (USS) sources (Jarvis et al. 2001).

Taking into account the point-source simulations from §4.1, we have estimated the distribution of spectral indices based on variations between injected/extracted flux densities. Assuming a radio population with $\alpha = -0.7$, and taking into account the uncertainties in the source extraction process, we predict that the spectral index distribution should broaden towards faint fluxes, reaching a scatter similar to that observed in our faintest flux density bins (see Table 7). These simulations are presented in parenthesis next to the observed results, and imply that the broad distribution of spectral indices is intrinsic above $S_{1.4GHz} \gtrsim 100 \mu\text{Jy}$ but dominated (broadened) by the fitting uncertainties (trumpet-like) at fainter flux densities.

Based on all sources, 6 per cent (<13 per cent) and 6 per cent (<9 per cent) have $\alpha > 0$ in the GMRT- and VLA-selected

catalogues, respectively (the fractions in parenthesis include upper/lower limits). Inspection by eye of these flat-spectrum sources reveals them to be compact at both wavelengths, brighter in the VLA image than in the GMRT image, probably due to synchrotron self-absorption in compact ($\lesssim 1$ kpc) GHz-peaked sources (Snellen et al. 2000) which are believed to be young FR II sources.

6 X-RAY IDENTIFICATIONS

Deep, hard X-ray observations (in the 2–10 keV band) provide an efficient method for identifying AGN (Mushotzky 2004), at least with column densities $N_H < 10^{24} \text{ cm}^{-2}$ (i.e. those that are ‘Compton thin’). Heavily absorbed AGN are common (Maiolino et al. 1998) and are expected to be responsible for the bulk of the cosmic X-ray background (CXRB; Ueda et al. 2003; Hasinger 2004; Gilli et al. 2007). Indeed, a large (~ 20 –50 per cent) fraction is believed to be Compton thick ($N_H > 10^{24} \text{ cm}^{-2}$), a population missed by even the deepest X-ray observations. Given that radio observations are unaffected by obscuration, this suggests that deep radio surveys may provide a method to find this missing population – the so-called QSO-2s.

In order to probe the nature of the sub-mJy radio population we have cross-matched our VLA 1.4-GHz catalogue (Table 4) with the deepest *XMM/Newton* image so far published (Brunner et al. 2008). The X-ray field has an area of 0.196 deg^2 (which is entirely covered by our VLA mosaic) and an effective exposure time of 637 ks. The X-ray catalogue contains 409 sources above a likelihood of 10 (3.9 σ) of which 266 and 340 are detected in the hard and soft X-ray band ($S_{2-10\text{keV}} \geq 9 \times 10^{-16} \text{ erg sec}^{-1} \text{ cm}^{-2}$, $S_{0.5-2\text{keV}} \geq 1.9 \times 10^{-16} \text{ erg sec}^{-1} \text{ cm}^{-2}$), respectively. The contamination by spurious sources in the X-ray catalogue is expected to be only ~ 1 per cent.

In Fig. 11 (left) we show the fraction of radio sources detected in the hard X-ray band – a good indicator for AGN activity – as a function of radio flux density. 32 per cent of the hard X-ray sample (85 sources) have a $> 5\sigma$ (PNR) 1.4-GHz detection, within 5 arcsec. This fraction declines from ~ 30 per cent at ~ 1 mJy to ~ 10 per cent at $\lesssim 100 \mu\text{Jy}$. A large number of faint radio sources, $S_{1.4GHz} < 300 \mu\text{Jy}$, that are detected in the hard X-ray band. This has been previously noted by Simpson et al. (2006), though in terms of the relative fraction they remain a minority.

The deeper radio and X-ray catalogues used in this work – compared to those used by Simpson et al. (where $S_{1.4GHz} \geq 100 \mu\text{Jy}$ and $S_{2-10\text{keV}} \gtrsim 3 \times 10^{-15} \text{ erg sec}^{-1} \text{ cm}^{-2}$ – Ueda et al. 2008) – do not show any clear evidence for a significant increase in the fraction of sources detected in X-rays at faint radio fluxes. Indeed, when we bin the X-ray data we find that between $S_{2-10\text{keV}} = 10^{-15} - 10^{-13} \text{ erg sec}^{-1} \text{ cm}^{-2}$, the fraction of X-ray sources detected in the radio image is relatively constant, ~ 35 per cent. For the faintest X-ray sources, only 25 per cent are detected in the radio image. We note that the use of a deeper, unpublished *XMM/Newton* catalogue (Mat Page, *private communication*) does not significantly modify the statistics at the faintest flux densities but increases (to 50 per cent) the fraction of counterparts at $S_{1.4GHz} \sim 1 \text{ mJy}$.

The Lockman Hole is a popular legacy field and a large number of the X-ray sources have been spectroscopically classified (e.g. Lehmann et al. 2001; Szokoly et al. 2009, in preparation). We use the compilation of Brunner et al. (2008) to plot the hard X-ray and 1.4-GHz flux densities (Fig. 11, right). Overplotted in the figure, we show the expected correlations between radio and X-ray fluxes for

610 MHz Flux Bin (mJy)	$\langle \alpha_{1.4\text{GHz}}^{610\text{MHz}} \rangle_{\text{ASURV}}$	Based on the 610 MHz-GMRT catalogue		
		$(\langle \alpha \rangle \pm \sigma_\alpha)_{\text{normal}}$	$(\langle \alpha \rangle \pm \sigma_\alpha)_{\text{biweight}}$	$\langle \langle \alpha_{1.4\text{GHz}}^{610\text{MHz}} \rangle \rangle_{\text{bootstrap}}$
6.00 – 40.00	-0.65 ± 0.05	-0.65 ± 0.22 (-0.70 ± 0.01)	-0.72 ± 0.15 (-0.70 ± 0.01)	-0.70 ± 0.04 (-0.70 ± 0.00)
1.50 – 6.00	-0.83 ± 0.09	-0.78 ± 0.47 (-0.70 ± 0.04)	-0.70 ± 0.33 (-0.70 ± 0.03)	-0.68 ± 0.06 (-0.70 ± 0.00)
0.50 – 1.50	-0.79 ± 0.06	-0.70 ± 0.42 (-0.74 ± 0.23)	-0.72 ± 0.31 (-0.71 ± 0.20)	-0.69 ± 0.04 (-0.72 ± 0.00)
0.20 – 0.50	-0.91 ± 0.03	-0.85 ± 0.40 (-0.80 ± 0.35)	-0.85 ± 0.38 (-0.77 ± 0.33)	-0.85 ± 0.04 (-0.77 ± 0.00)

1.4 GHz Flux Bin (mJy)	$\langle \alpha_{1.4\text{GHz}}^{610\text{MHz}} \rangle_{\text{ASURV}}$	Based on the 1.4 GHz-VLA catalogue		
		$(\langle \alpha \rangle \pm \sigma_\alpha)_{\text{normal}}$	$(\langle \alpha \rangle \pm \sigma_\alpha)_{\text{biweight}}$	$\langle \langle \alpha_{1.4\text{GHz}}^{610\text{MHz}} \rangle \rangle_{\text{bootstrap}}$
3.00 – 20.00	-0.59 ± 0.06	-0.59 ± 0.26 (-0.68 ± 0.02)	-0.67 ± 0.18 (-0.68 ± 0.02)	-0.63 ± 0.05 (-0.68 ± 0.00)
0.90 – 3.00	-0.48 ± 0.11	-0.48 ± 0.59 (-0.70 ± 0.04)	-0.64 ± 0.50 (-0.70 ± 0.04)	-0.60 ± 0.09 (-0.70 ± 0.00)
0.30 – 0.90	-0.51 ± 0.07	-0.61 ± 0.48 (-0.68 ± 0.18)	-0.67 ± 0.29 (-0.69 ± 0.17)	-0.65 ± 0.03 (-0.69 ± 0.00)
0.10 – 0.30	-0.48 ± 0.03	-0.57 ± 0.43 (-0.56 ± 0.55)	-0.59 ± 0.41 (-0.64 ± 0.45)	-0.60 ± 0.02 (-0.65 ± 0.00)

Table 7. Statistical properties of radio spectral indices as a function of flux density. These estimates are based on confident measures of the spectral indices, i.e. with no flags in Table 3 and 4. For both the 610-MHz- and 1.4-GHz-selected samples we use only $\geq 10\sigma$ (PNR) detections (but down to 5σ for the counterpart) to minimise the uncertainties from upper/lower limits. *Columns:* (1) the flux density bin; (2) the mean value given by the Kaplan-Meier product-limit estimator (ASURV – Feigelson & Nelson 1985) which takes into account the upper limits in the bin; (3) the mean and standard deviation of the spectral index distribution based on detections only; (4) the central location (mean) and scale parameter (sigma) based on the biweight estimator which is resistant to outliers and non-Gaussian distributions (Beers et al. 1990); (5) the median value of the distribution based on a bootstrap approach. The parentheses shown in some of the columns are the statistical estimates based on a single $\alpha = -0.7$ population with input/extracted flux ratios from the mock sources described in §4.1. These constitute a useful check on the reliability of the results, e.g. whether the observed scatter is intrinsic or dominated by errors.

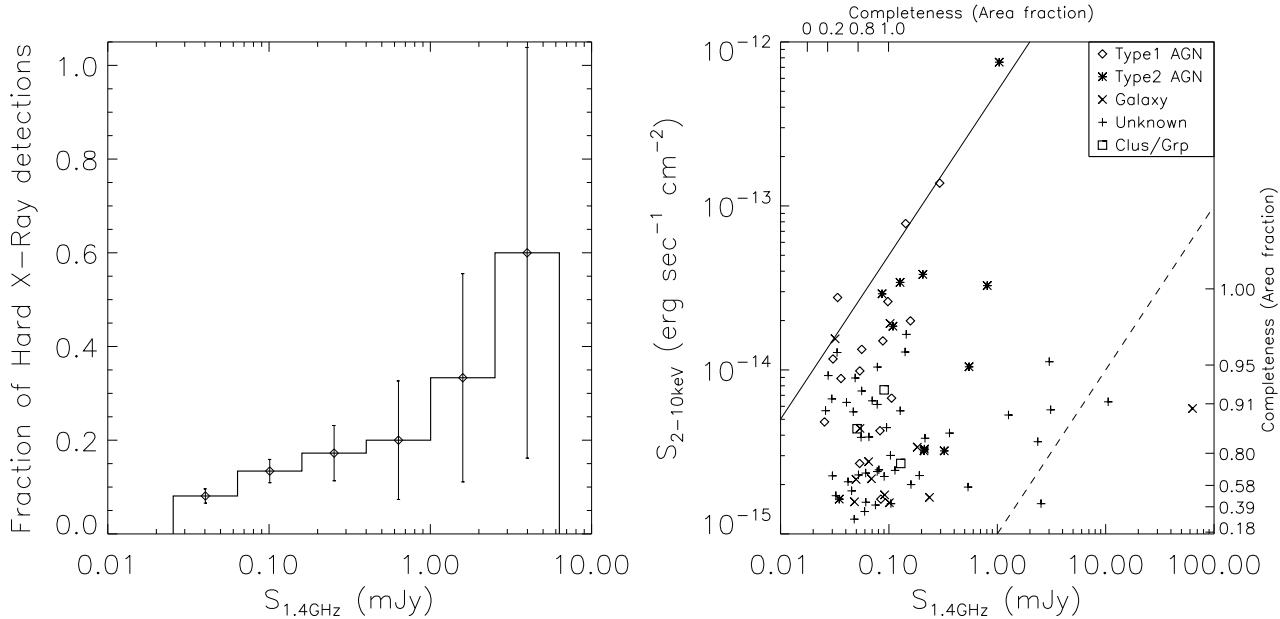


Figure 11. *Left:* The fraction of radio sources (at 1.4 GHz) detected by *XMM/Newton* in the hard X-ray band. Errors are assumed to be Poissonian. *Right:* Radio flux density versus X-ray flux density for cross-matched sources. The solid and dashed lines correspond to the expected correlation for radio-quiet AGN (Brinkmann et al. 2000) and star-forming galaxies (Condon 1992; Ranalli et al. 2003) introduced by Simpson et al. (2006), respectively. The different populations are based on spectroscopic identifications (Lehmann et al. e.g. 2001; Szokoly et al. e.g. 2009, in preparation) compiled by Brunner et al. (2008).

starbursts (Condon 1992; Ranalli et al. 2003) and radio-quiet AGN (Brinkmann et al. 2000) as dashed and solid lines, respectively. Deviations from these correlations can be produced by photoelectric absorption (lower X-ray fluxes) or by jets oriented close to our line of sight (larger radio fluxes).

We find that in the sub-mJy radio regime, the vast majority of the radio-quiet AGN (types 1 and 2) have $S_{2-10\text{keV}} \gtrsim 3 \times 10^{-15}$ erg sec $^{-1}$ cm $^{-2}$. This tallies with Simpson et al.’s criterion for identifying radio-quiet AGN, based on those sources lying closer to the solid than the dashed line in Fig. 11 (*right*). We find that the contamination produced by galaxies at fainter X-ray flux densities could be very large, since most of the spectroscopically iden-

tified galaxies lie at $S_{2-10\text{keV}} \lesssim 4 \times 10^{-15}$ erg sec $^{-1}$ cm $^{-2}$ – also in agreement with Simpson et al.’s criterion. Due to photoelectric absorption, the distribution of type-2 AGN has a large scatter in the hard X-ray band – they are typically found with radio fluxes, $S_{1.4\text{GHz}} \gtrsim 100 \mu\text{Jy}$. It is interesting to note the radio emission, at the $\sim 100\text{-}\mu\text{Jy}$ level, in two X-ray clusters (XMMUJ105339.7+573520, XMMUJ105346.4+573510) and one classified group (XMMUJ105318.9+572044).

From Fig. 11 (*right*) we find that the solid line (Brinkmann et al.’s correlation) appears to define an upper limit for the AGN population. The well-known radio-loud AGN population with $> 1 \text{ mJy}$ tends to agree better with the star-forming

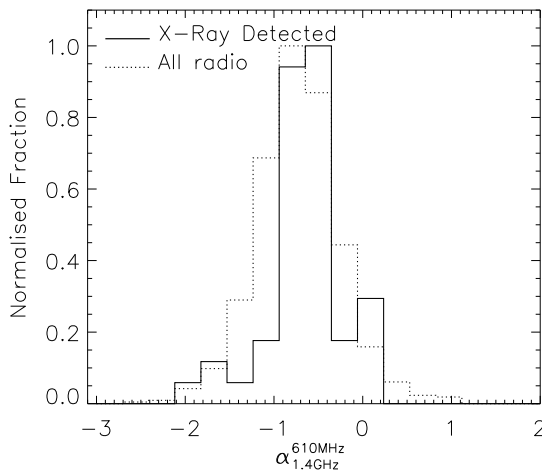


Figure 12. The radio spectral index between 610 MHz and 1.4 GHz for the sample of radio sources detected in the hard X-ray band.

galaxy correlation (*dashed line*). Finally, as the completeness functions indicate – *top* and *right* axes – the faintest radio/X-ray sources are observed in different areas of the map.

We have estimated the total fraction of radio-quiet AGN in the sub-mJy radio regime based on four assumptions: (1) the X-ray catalogue contains almost all the type-1 AGN in the redshift range of the radio sources (mean, $z \approx 0.8$); (2) to estimate an upper limit the spectroscopically-identified sources maintain the same relative fractions in the unknown population as in Fig. 11 (*right*); (3) a constant fraction of type 1/type 2 AGN = 1:4 based on X-ray observations of local Seyfert galaxies (e.g. Maiolino et al. 1998); (4) 25 per cent of the X-ray sources are Compton-thick (undetected, obviously) based on synthesis population models to reproduce the CXRB (e.g. Ueda et al. 2003).

We find that the number of classified type 1 AGN detected in both 1.4-GHz and X-ray wavebands is 21 (16 in the hard; 8 in the soft; 3 in both). These sources comprise 38 and 31 per cent of the spectroscopically classified samples (with radio detections) in the hard and soft X-ray bands, respectively. Considering the assumptions described above, we expect ~ 131 ($21 \times [1 + 4] \times [1 + 0.25]$) AGN in our radio sample, i.e. ~ 20 per cent of the 755 radio sources in the region covered in the X-ray waveband. Fig. 11 (*right*) clearly shows that most of the X-ray detections are at $S_{1.4\text{GHz}} \lesssim 300 \mu\text{Jy}$, therefore applying the same treatment we estimate that radio-quiet AGN compose a 19–37 and 19–30 per cent fraction of the $S_{1.4\text{GHz}} < 100 \mu\text{Jy}$ and $100 \mu\text{Jy} \leq S_{1.4\text{GHz}} < 300 \mu\text{Jy}$ radio population, respectively (upper limits based on the second assumption above). No strong variations for the content of radio-quiet AGN as a function of radio flux density are seen. These rough estimations are a little higher than previous Simpson et al.’s estimate, i.e. 10–20 per cent.

These results suggest a transition, at sub-mJy radio flux levels, from a bright and powerful AGN to a dominant star-forming galaxy population, contaminated at the $\sim 25 \pm 10$ per cent level by radio-quiet AGN.

Of the 84 hard X-ray sources detected at 1.4 GHz, 48 have a reliable radio spectral index (PNR > 5 in both 610 MHz and 1.4 GHz images). In Fig. 12 we plot $\alpha_{1.4\text{GHz}}^{610\text{MHz}}$ for the X-ray sources alongside those of the entire VLA sample. For the radio/X-ray sources, we find a median spectral index of -0.63 ± 0.04 , slightly

Class	N	$\langle\langle \alpha_{1.4\text{GHz}}^{610\text{MHz}} \rangle\rangle$
Type 1 AGN	9	-0.79 ± 0.20
Type 2 AGN	8	-0.60 ± 0.12
Galaxy	6	-0.65 ± 0.26
Unknown	24	-0.58 ± 0.07
Cluster/Group	1	-1.87

Table 8. The median (bootstrap) radio spectral index for the spectroscopically identified hard X-ray sources plotted in Fig. 11 (*right*).

flatter than that of the whole 1.4-GHz sample (-0.70 ± 0.01). A Kolmogorov-Smirnov test gives a probability of 16 per cent that both populations come from the same parent distribution. The spectral indices for the spectroscopically identified X-ray populations are presented in Table 8. Given that most of the sources are found at faint radio fluxes, these values may be highly biased by incompleteness at 610 MHz.

We conclude that radio-quiet AGN are no more numerous than star-forming galaxies at faint flux densities. The fraction of radio sources harbouring an AGN decreases towards faint radio flux densities – a transition from radio-loud AGN to a dominant star-forming galaxy population at sub-mJy radio fluxes.

7 DISCUSSION

7.1 Comparison with a previous 610-MHz survey

Garn et al. (2008b) published a $6-\sigma$ 610-MHz catalogue covering 5 deg^2 in the Lockman Hole using GMRT. This allows a direct comparison with our detections at 610 MHz. The Garn et al. mosaic ($\sigma_{610\text{MHz}} \sim 60 \mu\text{Jy beam}^{-1}$) covers the north-western portion of our GMRT mosaic, with $\sim 0.6 \text{ deg}^2$ in common. Cross-matching their catalogue with ours reveals good agreement in flux densities for the brightest detections. However, we find a very large number of spurious, faint sources in their catalogue. In Fig. 13 (*top*) we show the fraction of Garn et al. sources which are recovered (within 7 arcsec) in our $4 \times$ deeper image, as a function of their radio flux densities. Given the depth of our image, we expect all Garn et al. sources should have a counterpart in our catalogue, but no hints of emission in the image (Fig. 13 – *bottom*) are found for the vast majority of their $\lesssim 3 \text{ mJy}$ (PNR $\lesssim 10$) sources. We conclude that Garn et al. (2008b) have not provided a reliable $6-\sigma$ catalogue. It is interesting to note, however, that the number counts presented in Fig. 8 are in agreement with ours, probably because they base their number counts considering bright sources ($\gtrsim 10-\sigma$) in the cleanest regions of their map only.

Looking at the full Garn et al. Lockman Hole image, their sources lie mainly near the edge of their pointings, where the noise levels are greatest. The cleanest areas of their image contain very few sources, suggesting that their source extraction did not utilise knowledge of the local noise level. The distribution of 610-MHz sources in the *Spitzer* FLS (Garn et al. 2007, as used by Magliocchetti et al. 2008) appears similar, with a dearth of sources in the deepest portion of the mosaic (see figure 1 of Magliocchetti et al. 2008). This suggests that some of the faint steep-spectrum emitters seen by Magliocchetti et al. may be spurious (by random association), and that their spectral index distribution is likely broadened at faint flux densities.

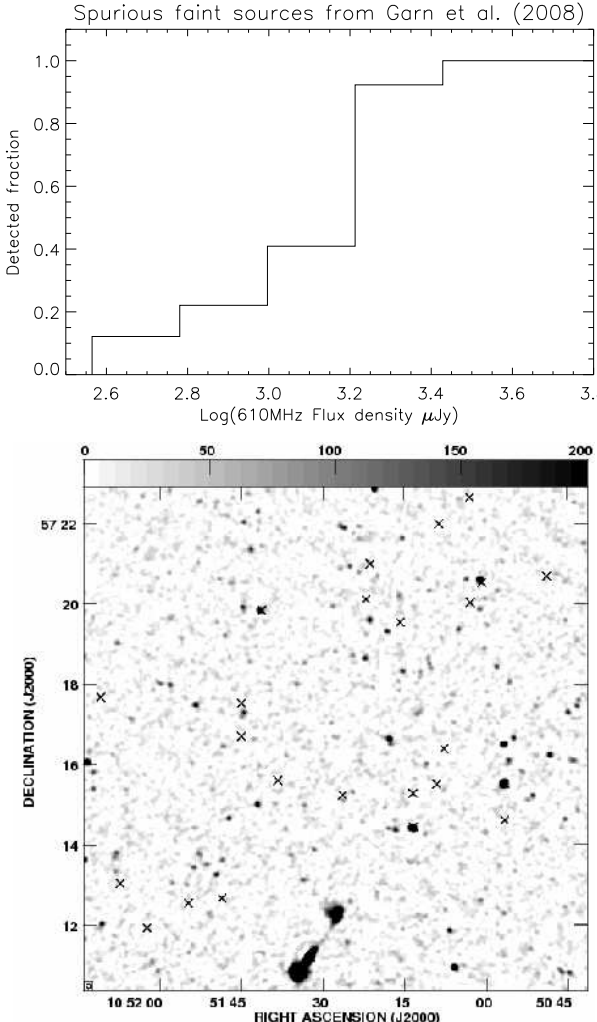


Figure 13. *Top:* Fraction of Garn et al. (2008b) sources recovered in our image as a function of their 610-MHz flux density. *Bottom:* An area of 12×12 arcmin 2 from our 610-MHz mosaic shown in grey-scale with a linear stretch from 0–200 $\mu\text{Jy beam}^{-1}$. Crosses show source positions catalogued by Garn et al. (2008b). We expect detections of all their sources since they have $S_{610\text{MHz}}^{\text{Garn}} > 300 \mu\text{Jy}$.

7.2 Comparison with a previous 1.4-GHz catalogue

Biggs & Ivison (2006) used some of the VLA data utilised in this paper. They present a high-resolution (A-configuration) map with a ~ 1.3 -arcsec beam (FWHM), and a different method of source detection. We find our work yields slightly higher flux densities. The mean flux density ratio, $S_{1.4\text{GHz}}^{\text{ours}}/S_{1.4\text{GHz}}^{\text{Biggs}}$, is 1.16 ± 0.02 (88 sources) with a standard deviation of 0.15 for cross-matched sources with peak-to-noise ratio higher than 15. We have demonstrated in §4.3 that this difference is not produced by calibration problems from adding A- and B-configuration data. A detailed analysis of both samples has been carried out and we have found that differences in flux are produced by the different approaches to source extraction. In particular, Biggs & Ivison (2006) used a fixed beam size to fit a Gaussian to sources which were first extracted with areas smaller than the beam. This results in lower measured flux densities, as seen in Fig. 14. Reducing all our 1.4-GHz fluxes by a factor $1.16\times$ would decrease the observed spectral indices (numerically) by 0.18 (i.e. the spectra become steeper), but we stress

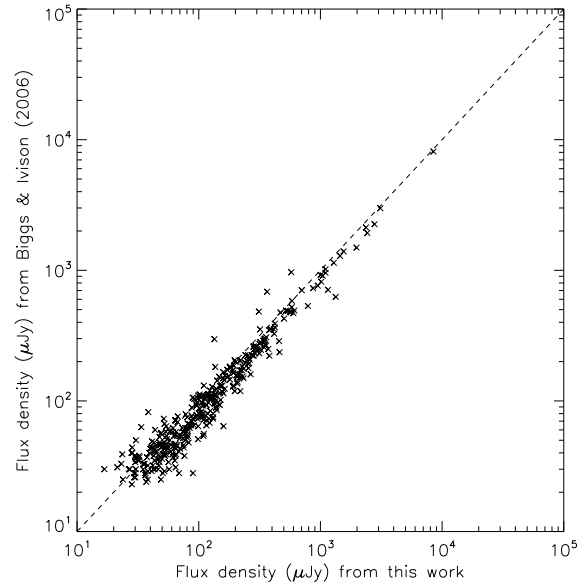


Figure 14. Integrated flux densities for the sources detected in the Lockman Hole at 1.4GHz in comparison with a previous work by Biggs & Ivison (2006). Sources have been cross-matched using a search radius of 4.2 arcsec.

that this would not affect the (absence of) trend in the spectral index distribution towards faint flux densities, nor the width of the observed α distribution.

7.3 Previous spectral index studies

The radio spectral index observed between 610 MHz and 1.4 GHz has been controversial since the earliest studies. Using the WSRT, Katgert & Spinrad (1974) found – from a small sample of sources with $S_{610\text{MHz}} \gtrsim 10 \text{ mJy}$ – a spectral index distribution, $\alpha_{1.4\text{GHz}}^{610\text{MHz}} = -0.52 \pm 0.39$, an unusual result with a broad distribution with respect to higher frequency surveys. A much larger sample gave a similar result: $\alpha_{1.4\text{GHz}}^{610\text{MHz}} = -0.68 \pm 0.31$ (Katgert 1979), statistically in agreement with the previous work, but showing clear evidence for more complex than single power law spectra. Our survey covers only $\sim 1 \text{ deg}^2$ and therefore contains a small number (18) of sources in the $S_{610\text{MHz}} \gtrsim 10 \text{ mJy}$ range. From these sources, 12 have got a reliable radio spectral index from which we find a mean $\langle \alpha \rangle \approx -0.71$ and standard deviation of $\sigma_\alpha \approx 0.17$, in agreement with early results but with a considerably tighter distribution. Since these sources are mostly powerful steep-spectrum radio-loud AGN (Hopkins et al. 2000), we have also compared these spectral indexes with a sample of $z < 0.5$ FR II sources ($\alpha_{750\text{MHz}}^{178\text{MHz}} = 0.79 \pm 0.14$, mean and scatter), finding good agreements as well (Laing et al. 1983).

With the advent of the GMRT, a variety of spectral index results have appeared in the literature. They cover different flux density ranges, so we present in Table 9 a comparison using the same ranges. We find good agreement – within the errors – with the estimates of Bondi et al. (2007) and Tasse et al. (2007), although not with Garn et al. (2008a), probably because of faint spurious associations (discussed in §7.1) or incompleteness in their estimations.

Flux range (mJy)	$\langle\langle \alpha_{1.4\text{GHz}}^{610\text{MHz}} \rangle\rangle^{\text{Ref}}$	$\langle\langle \alpha_{1.4\text{GHz}}^{610\text{MHz}} \rangle\rangle^{\text{Ours}}$
$0.5 < S_{1.4\text{GHz}}$	$-0.67 \pm 0.05^{(1)}$	-0.63 ± 0.03
$0.15 < S_{1.4\text{GHz}} < 0.5$	$-0.46 \pm 0.03^{(1)}$	-0.63 ± 0.02
$0.1 < S_{1.4\text{GHz}} < 0.15$	$-0.61 \pm 0.04^{(1)}$	-0.59 ± 0.03
$1.0 < S_{610\text{MHz}}$	$-0.56 \pm 0.04^{(2)}$	-0.69 ± 0.04
$0.5 < S_{610\text{MHz}} < 1.0$	$-0.36 \pm 0.12^{(2)}$	-0.71 ± 0.04
$30 < S_{610\text{MHz}}$	$-0.76^{(3)}$	-0.71 ± 0.17

Table 9. A direct comparison of our results with previous work on the spectral index between 610 MHz and 1.4 GHz: (1) Bondi et al. (2007); (2) Garn et al. (2008a); (3) Tasse et al. (2007). The double parentheses enclose median values, where we estimate our errors using a bootstrapping analysis.

7.4 The nature of the sub-mJy radio emitters

There is little agreement in the literature concerning the optical properties of sub-mJy radio sources. Some studies support the idea that faint radio emitters are primarily star-forming galaxies. The spectroscopic classification of $S_{1.4\text{GHz}} \gtrsim 40\text{-}\mu\text{Jy}$ sources by Barger et al. (2007) shows that the dominant population has strong Balmer lines and no broad or high-ionisation lines. Likewise, Bondi et al. (2007) find that late-type starbursts dominate the $S_{1.4\text{GHz}} \lesssim 100\text{-}\mu\text{Jy}$ regime based on analysis of an optical colour-colour plot (Ciliegi et al. 2005). Work based on a morphological classification in the optical (Padovani et al. 2007) shows that star-forming galaxies comprise only about a third of the sub-mJy population. More radically, based on another optical colour-colour study, Simpson et al. (2006) presented evidence for no change in the composition of the radio source population towards faint flux densities, arguing for a dominant passively-evolving massive elliptical galaxy population at all flux levels, $S_{1.4\text{GHz}} \gtrsim 100\text{-}\mu\text{Jy}$. On the other hand, at $\sim 100\text{-}\mu\text{Jy}$, bright submillimetre-selected galaxies – which are very clearly dominated by star formation – make up a significant number of the optically faint radio emitters (Ivison et al. 2002; Pope et al. 2006).

The approaches taken by all these studies reflect the difficulty of disentangling star-forming galaxies from nuclear AGN activity.

We note that the large scatter ($\sigma_\alpha \approx 0.4$) seen in Fig. 9 for the spectral indices suggests a more complicated scenario than a simple star-forming galaxy population (e.g. see Fig. 11, right). We have found that the use of radio spectral index as a probe of a galaxy's nature is highly degenerate: supernova remnants and nuclear activity are closely related (Gebhardt et al. 2000); redshift effects may be combined with synchrotron losses, steepening the spectra (Jarvis et al. 2001) and – given the poor resolution of our images – spectral indices cannot be obtained for resolved components. Therefore, a galaxy's nature is difficult to disentangle using only the radio spectral index. Nevertheless, in this work we find that the sub-mJy radio population is characterised by optically-thin synchrotron emission, contaminated at the $\sim 25 \pm 10$ per cent level by radio-quiet AGN – based on X-ray detections and previous spectroscopic classifications – in rough agreement with a previous study by Simpson et al. (2006).

8 CONCLUDING REMARKS

We have observed the Lockman Hole field using the GMRT at 610 MHz and the VLA at 1.4 GHz, obtaining two deep radio im-

ages with similar spatial resolutions and well-matched noise levels (15 and $6\text{-}\mu\text{Jy beam}^{-1}$, respectively) – the former representing the deepest GMRT image yet published. The data reveal a flattening followed by a second peak in the Euclidean-normalised number counts in the sub-mJy radio regime – evidence for the appearance of a different radio population dominating these faint flux densities.

We discuss the reliability of the 610-MHz catalogue presented by Garn et al. (2008b) in the Lockman Hole, finding that their catalogue is highly contaminated by spurious sources, with similar problems apparent in their previous *Spitzer* FLS catalogue (Garn et al. 2007). This may have influenced the detection of steep-spectrum radio emitters reported by Magliocchetti et al. (2008).

We study the spectral index of the radio emitters by combining our GMRT and the VLA measurements. The GMRT data are about $4\times$ times deeper than previous imaging, allowing for clean results and avoiding the well-known bias for steeper- or flatter-spectrum sources in samples selected at longer or shorter wavelengths, respectively. Analyses show evidence for large capabilities from GMRT observations for imaging steep-spectrum steep-spectrum sources in the field. Indeed, approximately 30 per cent of the GMRT sources are undetected at 1.4 GHz, revealing the sensitivity of deep 610-MHz images to faint, high-redshift star-forming galaxies such as those detected in submillimetre surveys (e.g. Ivison et al. 2007).

Our results, based on $\geq 10\sigma$ selection criterion, show that the mean and median spectral index does not evolve as a function of radio flux density, certainly between $\sim 100\text{-}\mu\text{Jy}$ and 10-mJy at 1.4 GHz. We find $\alpha_{1.4\text{GHz}}^{610\text{MHz}} \approx -0.6$ to -0.7 , which suggests that optically-thin synchrotron emission is the dominant emission mechanism in the sub-mJy population. The two most probable contributors are star-forming galaxies and Fanaroff & Riley sources, ruling out a possible dominant flat-spectrum population (AGN-cores; GPS) at these faint flux densities (Bondi et al. 2007; Garn et al. 2008a).

We find the distribution of spectral indices has a significant scatter ($\sigma_\alpha \approx 0.4$), which suggests a complicated scenario where different populations mix together. The fraction of inverted-spectrum ($\alpha > 0$) sources is just 6 per cent ($\lesssim 11$ including lower limits) of the total sample.

Based on X-ray observations with spectroscopic classifications (Brunner et al. 2008), we estimate that approximately $\sim 25 \pm 10$ per cent of the radio sample is made up of radio-quiet AGN at $30\text{-}\mu\text{Jy} \lesssim S_{1.4\text{GHz}} < 300\text{-}\mu\text{Jy}$, with this fraction rising towards brighter flux densities. These results suggest a transition from AGN to a dominant star-forming population at sub-mJy radio fluxes.

ACKNOWLEDGEMENTS

This paper was supported by a Gemini-STFC research studentship. We thank the staff of the GMRT that made these observations possible.

REFERENCES

- Barger A. J., Cowie L. L., Wang W.-H., 2007, ApJ, 654, 764
- Beers T. C., Flynn K., Gebhardt K., 1990, AJ, 100, 32
- Biggs A. D., Ivison R. J., 2006, MNRAS, 371, 963
- Biggs A. D., Ivison R. J., 2008, MNRAS, 385, 893
- Blundell K. M., Kuncic Z., 2007, ApJ, 668, L103
- Bondi M. et al., 2007, A&A, 463, 519

- Bondi M. et al., 2003, A&A, 403, 857
- Brinkmann W., Laurent-Muehleisen S. A., Voges W., Siebert J., Becker R. H., Brotherton M. S., White R. L., Gregg M. D., 2000, A&A, 356, 445
- Brunner H., Cappelluti N., Hasinger G., Barcons X., Fabian A. C., Mainieri V., Szokoly G., 2008, A&A, 479, 283
- Chambers K. C., Miley G. K., van Breugel W. J. M., Bremer M. A. R., Huang J.-S., Trentham N. A., 1996, ApJS, 106, 247
- Ciliegi P. et al., 1999, MNRAS, 302, 222
- Ciliegi P. et al., 2005, A&A, 441, 879
- Clemens M. S., Vega O., Bressan A., Granato G. L., Silva L., Panuzzo P., 2008, A&A, 477, 95
- Condon J. J., 1992, ARA&A, 30, 575
- Condon J. J., 1997, PASP, 109, 166
- Condon J. J., 2007, in Astronomical Society of the Pacific Conference Series, Vol. 380, Afonso J., Ferguson H. C., Mobasher B., Norris R., eds, Deepest Astronomical Surveys, p. 189
- Condon J. J., Cotton W. D., Yin Q. F., Shupe D. L., Storrie-Lombardi L. J., Helou G., Soifer B. T., Werner M. W., 2003, AJ, 125, 2411
- Donley J. L., Rieke G. H., Rigby J. R., Pérez-González P. G., 2005, ApJ, 634, 169
- Fanaroff B. L., Riley J. M., 1974, MNRAS, 167, 31P
- Feigelson E. D., Nelson P. I., 1985, ApJ, 293, 192
- Fixsen D. J. et al., 2009, ArXiv e-prints
- Garn T., Green D. A., Hales S. E. G., Riley J. M., Alexander P., 2007, MNRAS, 376, 1251
- Garn T., Green D. A., Riley J. M., Alexander P., 2008a, MNRAS, 383, 75
- Garn T., Green D. A., Riley J. M., Alexander P., 2008b, MNRAS, 387, 1037
- Garrett M. A., Wrobel J. M., Morganti R., 2005, ApJ, 619, 105
- Gebhardt K. et al., 2000, ApJ, 539, L13
- Gehrels N., 1986, ApJ, 303, 336
- Gervasi M., Tartari A., Zannoni M., Boella G., Sironi G., 2008, ApJ, 682, 223
- Gilli R., Comastri A., Hasinger G., 2007, A&A, 463, 79
- Gopal-Krishna , Patnaik A. R., Steppe H., 1983, A&A, 123, 107
- Gruppioni C., Mignoli M., Zamorani G., 1999, MNRAS, 304, 199
- Hasinger G., 2004, Nuclear Physics B Proceedings Supplements, 132, 86
- Hopkins A., Windhorst R., Cram L., Ekers R., 2000, Experimental Astronomy, 10, 419
- Hopkins A. M., Afonso J., Chan B., Cram L. E., Georgakakis A., Mobasher B., 2003, AJ, 125, 465
- Ibar E. et al., 2008, MNRAS, 386, 953
- Ivison R. J. et al., 2007, MNRAS, 380, 199
- Ivison R. J. et al., 2002, MNRAS, 337, 1
- Jarvis M. J. et al., 2001, MNRAS, 326, 1563
- Katgert J. K., 1979, A&A, 73, 107
- Katgert J. K., Spinrad H., 1974, A&A, 35, 393
- Katgert-Merkelijn J. K., Windhorst R. A., Katgert P., Robertson J. G., 1985, AAPS, 61, 517
- Laing R. A., Riley J. M., Longair M. S., 1983, MNRAS, 204, 151
- Lehmann I. et al., 2001, A&A, 371, 833
- Magliocchetti M., Andreani P., Zwaan M. A., 2008, MNRAS, 383, 479
- Maiolino R., Salvati M., Bassani L., Dadina M., della Ceca R., Matt G., Risaliti G., Zamorani G., 1998, A&A, 338, 781
- Matthews T. A., Morgan W. W., Schmidt M., 1964, ApJ, 140, 35
- Mitchell K. J., Condon J. J., 1985, AJ, 90, 1957
- Morrison et al. , in preparation
- Moss D., Seymour N., McHardy I. M., Dwelly T., Page M. J., Loaring N. S., 2007, MNRAS, 378, 995
- Mushotzky R., 2004, in Astrophysics and Space Science Library, Vol. 308, Barger A. J., ed, Supermassive Black Holes in the Distant Universe, p. 53
- Muxlow T. W. B. et al., 2005, MNRAS, 358, 1159
- O'Dea C. P., 1998, PASP, 110, 493
- Owen F. N., Morrison G. E., 2008, AJ, 136, 1889
- Padovani P., Mainieri V., Tozzi P., Kellermann K. I., Fomalont E. B., Miller N., Rosati P., Shaver P., 2007, in Astronomical Society of the Pacific Conference Series, Vol. 380, Afonso J., Ferguson H. C., Mobasher B., Norris R., eds, Deepest Astronomical Surveys, p. 205
- Pope A. et al., 2006, MNRAS, 370, 1185
- Ranalli P., Comastri A., Setti G., 2003, A&A, 399, 39
- Richards E. A., 2000, ApJ, 533, 611
- Röttgering H., Snellen I., Miley G., de Jong J. P., Hanisch R. J., Perley R., 1994, ApJ, 436, 654
- Seymour N. et al., 2008, MNRAS, 386, 1695
- Seymour N., McHardy I. M., Gunn K. F., 2004, MNRAS, 352, 131
- Simpson C. et al., 2006, MNRAS, 372, 741
- Smolčić V. et al., 2008, ApJS, 177, 14
- Snellen I. A. G., Schilizzi R. T., Miley G. K., de Bruyn A. G., Bremer M. N., Röttgering H. J. A., 2000, MNRAS, 319, 445
- Szokoly et al. , in preparation
- Tasse C., Röttgering H. J. A., Best P. N., Cohen A. S., Pierre M., Wilman R., 2007, A&A, 471, 1105
- Taylor G. B., Carilli C. L., Perley R. A., eds, 1999, Astronomical Society of the Pacific Conference Series, Vol. 180, Synthesis Imaging in Radio Astronomy II
- Ueda Y., Akiyama M., Ohta K., Miyaji T., 2003, ApJ, 598, 886
- Ueda Y. et al., 2008, ApJS, 179, 124
- Valentijn A. E., 1980, A&A, 89, 234
- Valentijn E. A., Jaffe W. J., Perola G. C., 1977, AAPS, 28, 333
- Windhorst R., Mathis D., Neuschaefer L., 1990, in Astronomical Society of the Pacific Conference Series, Vol. 10, Kron R. G., ed, Evolution of the Universe of Galaxies, p. 389
- Windhorst R. A., Miley G. K., Owen F. N., Kron R. G., Koo D. C., 1985, ApJ, 289, 494
- Wrobel J. M., Taylor G. B., Rector T. A., Myers S. T., Fassnacht C. D., 2005, AJ, 130, 923

This paper has been typeset from a \TeX / \LaTeX file prepared by the author.